High-Power Microwave Sources

Victor L. Granatstein
and
Igor Alexeff, Editors

Artech House
Boston • London

Chapter 13

VIRTUAL CATHODE OSCILLATOR (VIRCATOR) THEORY

Donald J. Sullivan

Mission Research Corporation
Albuquerque, New Mexico

John E. Walsh

Department of Physics and Astronomy
Dartmouth College
Hanover, New Hampshire

Evangelos A. Coutsias

Department of Mathematics and Statistics
University of New Mexico
Albuquerque, New Mexico

13.1 INTRODUCTION

Since the discovery of the Child-Langmuir relation [1, 2], it has been known that exceeding the limiting current of a diode leads to the development of a *virtual cathode*. Subsequently, numerous papers were written on experiments and theory relating to space-charge-limited flows. Birdsall and Bridges [3] provide an excellent background and bibliography. More recently, the exact steady-state solutions for electron beams in one-dimensional relativistic diodes [4] and bounded drift spaces [5] were derived in the US and USSR. We can easily see that for sufficiently large currents there are two steady states for an electron beam, only one of which is

stable [6]. These two states coalesce at the *space-charge limit* (SCL), and above it they disappear [7]. As current is increased above the SCL, the beam developes a jump instability and relaxes into an oscillating state.

In the early 1960s, computer models were developed, which quantitatively depicted the nonlinear oscillatory nature of the virtual cathode [8–10]. These were one-dimensional, non-relativistic, electrostatic, multiple-sheet models. Birdsall and Bridges [8, 9] qualitatively pointed out many interesting dependencies of the oscillation frequency and the potential minimum position on injected current, thermal spread, and circuit resistance. Dunn and Ho [10] present computer experiments with one and two species.

The phenomenon of virtual cathode formation in intense relativistic electron beams figures prominently in a number of high-interest research areas. Devices used to produce high-current ion beams for inertial confinement fusion—*pinch reflex diode* [11, 12] and *reflex triodes* [13, 14]—depend on the virtual cathode to inhibit electron transport, and use the cathode's potential well to accelerate ions. The recent concept of the *spherical electron-to-ion converter* [15] requires a virtual cathode.

The virtual cathode plays a dominant role in areas other than production of light ion beams for fusion. The virtual cathode is attributed with the main role in collective ion acceleration in neutral gas [16, 17]. Control of virtual cathode motion is the mechanism for acceleration in the *ionization front accelerator* [18, 19] and also in two concepts for *collective-effect accelerators* [20, 21]. However, the virtual cathode's most interesting application is its use in producing high-power centimeter and millimeter wavelength microwaves [22–36]. Experiments using reflex triodes have already produced GW power levels with 12% beam-to-RF efficiency [25]. This application of the virtual cathode will be considered in the present chapter.

The *virtual cathode oscillator* (vircator) in its modern form is an essentially new class of microwave tube. The vircator has the attribute of conceptual simplicity, high-output-power capacity, and wide tuning ability. Experimental work [22–25, 31–36] and the results of particle code simulations [26–31] clearly indicate that the vircator is a source of extraordinarily high power. Some of these experimental results are listed in Table 13.1. Hence, the vircator has some unique applications. The long-term success of the vircator will be measured in part by the position that the device takes in the competitive ranks of standard microwave tubes [37], but in the shorter term the demonstrated success of preliminary experiments assures that vircators will be used for things other than microwave tube research.

The development of sources in the microwave range of the spectrum is a pursuit that almost dates from the origin of modern electromagnetic theory [38], and precursors [39–41] of the modern vircator can be found

Table 13.1 Results of Vircator Experiments

Reference	*System*	*Peak Power*	*Frequency**	*Efficiency*
Mahaffey, *et al.*	Reflex Triode	100 MW	11 GHz (10.0–12.4 GHz)	1.5%
Brandt, *et al.*	Reflex Triode	1 GW	9.8 GHz (7.0–13.0 GHz)	2.0%
Buzzi, *et al.*	Foil Diode	1 GW	10 GHz (9.0–14.0 GHz)	1.25%
Didenko, *et al.*	Reflex Triode	1.4 GW	3.3 GHz (2.1–5.0 GHz)	12%
Scarpetti, *et al.*	Foil Diode	300 MW	6.9 GHz (5.3–12.4 GHz)	1.6%
Clark *et al.*	Foil Diode	1 GW	2–10 GHz Tuned	2.0%
Didenko, *et al.*	Reflex Triode	600 MW	(1.4–18.0 GHz) 3.3 GHz	50%

*Detector bandwidth in parentheses.

in the early short-wavelength results of literature in vacuum tube research. During the course of 40 to 50 years of intensive research and development in microwave technology, a very great variety of conceptual approaches have been introduced for the production of electron-beam-generated coherent radiation. A relative few of these have survived, been reduced to practice, and put in a form that can be routinely used in applications. Recent additions to the family are gyrotrons [42] and, possibly, the general class of free-electron lasers [43, 44].

Each successful addition is based in part on a development that relaxes a constraint or expands the general parameter space available for electron beam bunching. In the case of the vircator, the availability of convenient high-power, high-voltage, low-impedance electron beam generators plays a key role. Single-pulse generators of very high peak power have been used in vircator research [22–25, 31–36], and compact, high-power, high-repetition-rate pulsers with suitable beam parameters have been demonstrated for vircator operation [45]. The development of these pulsers is essential to more routine use of the vircator mechanism, and therefore it has a good chance of becoming a standard approach in some applications [46].

The performance of microwave tubes can be summarized in part by a number of general scaling laws. One of these, which is useful in assessing the comparative performance of the vircator, is the relation between output power and operating frequency:

$$P_o = P_r \left(\frac{f_r}{f_o}\right) \alpha$$

where the subscripts r and o stand for reference and output, respectively. The parameter α [47] is a positive number, which for standard microwave tubes, lies in the range of 2–4. If a reference frequency, f_r = 10 GHz is adopted, high-power klystron or magnetron technology will typically have P_r in the .1–1 MW range. Experiment [45] has shown that, when driven by a power supply of comparable size, a vircator can easily achieve a power (at 10 GHz) near or above the upper end of this range. Furthermore, the vircator in this range also has a demonstrated wide tuning ability (mechanical tuning of 50% bandwidth has been achieved). Neither the klystron nor the magnetron have this tuning capability. High-power coupled-cavity TWTs have a pulsed peak power limit near the lower end of the stated output power range, and sources of this type will have a more limited bandwidth. Helical TWTs will have a high fractional bandwidth, but the power level available at 10 GHz is typically much smaller (10 kW). However, the TWT is generally used as an amplifier, and vircator-amplifier operation has not yet been demonstrated by experiment.

In a closed-cavity tube (klystron, magnetron, coupled-cavity TWT), the parameter α is generally near the middle to upper end of the range α = 2–4, while α is generally smaller in the more open structure (at least one dimension much greater than the operating wavelength). The vircator has a potentially large mode volume [35] (operating wavelength cubed greater than or equal to the interaction volume), and hence it to may decline with frequency at a comparatively slow rate. However, the scaling of the vircator mechanism has not yet been demonstrated over multidecades in frequency. Hence, its competitive position with respect to the gyrotron is not yet fully established, and gyrotron sources, when operated at millimeter wavelengths may exceed by as much as two orders of magnitude the output power available from other standard tubes. As compared with a gyrotron, however, a vircator is based on a simpler technology, and hence may be an attractive option for some millimeter-wavelength applications.

In summary, the results of research to date support the claim that a vircator can perform at or above the level of standard microwave tubes. Anticipated power levels and operating frequencies of the vircator relative to other short-pulse microwave tubes are shown in Figure 13.1.

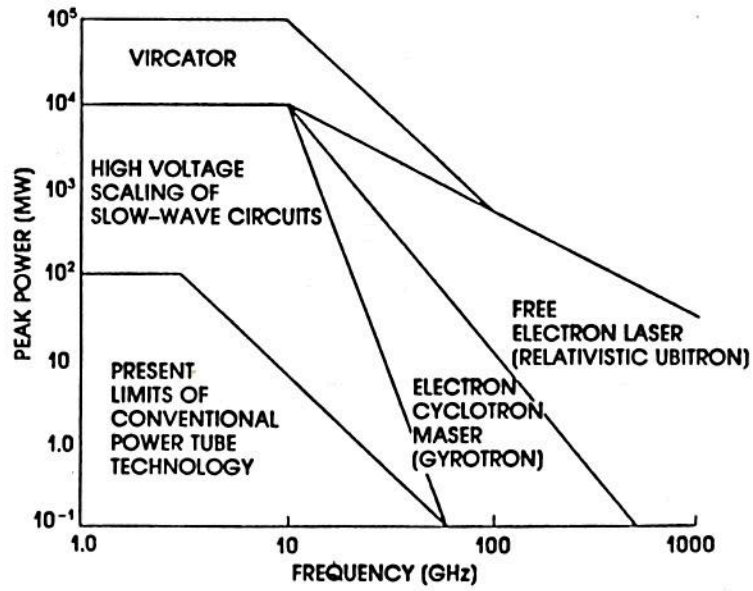

Fig. 13.1 Projected Limits of Ultra-High-Power Microwave Source (<100 ns) Technology (Courtesy of R. Parker).

13.2 THE SPACE-CHARGE-LIMITING CURRENT

13.2.1 Theory

The concept of limiting current can be visualized in the following, oversimplified physical picture. As particles from the electron beam (see Figure 13.2) enter the drift tube, the charge which they carry creates a potential barrier against further transmission of current. If the injected current is greater than the limiting current, the potential energy $e\Phi$ will exceed the kinetic energy of the beam $(\gamma_0 - 1)mc^2$, where

e = electron charge;
Φ = electrostatic potential ≤ 0;
γ = relativistic factor $(1 - \beta^2)^{-1/2}$;
γ_0 = value of γ at injection;
β = v/c;
v = electron velocity;
m = electron rest mass.

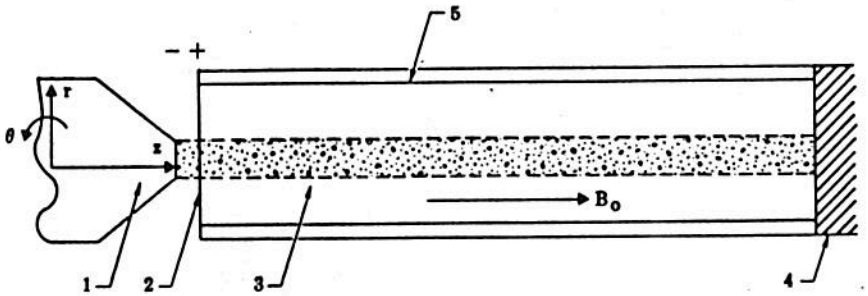

Fig. 13.2 Schematic of an Electron Beam: (1) Cathode; (2) Anode; (3) Drift Space; (4) Collector; (5) Return Current Conductor
Note: The principal coordinate axes z, r, and θ are shown.

At that position, the barrier is large enough to stop the current and cause reflection of beam electrons. Thus, the deep potential well is called a *virtual cathode*. Note, however, that because the amplitude of the well fluctuates in time and space, the beam is never completely cut off by the virtual cathode.

The general space-charge-limiting current problem does not lend itself to analytical solution. Instead, theoretical work on the subject has attempted to solve for limiting currents, which develop in electron beams,

in the strictly electrostatic case. The solutions derived are only valid for beams in steady-state equilibrium (i.e., $I < I_{SCL}$). (The subscript SCL denotes the space-charge limit.) Also, the derivations depend on the following assumptions.

(1.) The electron beam is a cold plasma, $T_e = 0$ which implies the electrons are collisionless, and allows us to neglect the $\vec{\nabla}P_e$ and viscosity terms in the momentum transfer equation. Here, T_e is the electron temperature and P_e is the electron pressure.

(2.) The electron beam is axially homogeneous and infinite. In real terms the infinite-beam assumption implies $L \gg R$, where L is the drift tube length and R is the drift tube radius. This allows the beam to reach a steady state far enough downstream from the injection plane to make the equilibrium beam density n_b^0, velocity $\vec{v}^0$, and electric field $\vec{E}^0$, independent of z.

(3.) The equilibrium radial density and velocity profiles are azimuthally symmetric about the magnetic axis. In conjunction with assumption 2 this means that n_b^0, $\vec{v}^0$, and $\vec{E}^0$ are functions only of the radial distance r.

(4.) The electron particle density and kinetic energy are independent of r at the anode plane. Therefore, the beam is uniform in space and monoenergetic at injection into the drift tube; anode foil scattering is neglected.

(5.) The externally imposed longitudinal magnetic field $\vec{B}_0$ is effectively infinite. If this assumption is not made, the current-induced-equilibrium self-magnetic fields would play a major role in determining the equilibrium radial profile of the beam. Because $\vec{B}_0$ is taken as infinite, it guides the electrons and contains them, and hence the self-fields can be treated as perturbations. Another way of expressing this assumption is to state that the Larmor radius of an electron in the $\vec{B}_0$ field must be much less than the beam radius, $r_L \ll r_0$.

Because assumptions 1 through 5 reduce the problem to the electrostatic case, solving Poisson's equation will give the desired result. By using this approach, several researchers have derived expressions for the space-charge-limited current of electron beams in vacuum and in charge-neutral plasmas. Excellent reviews have been written [48, 49], and the most widely cited results are those of Bogdankevich and Rukhadze [48]. By using the conservation of energy and momentum, these authors were able to write Poisson's equation for a cylindrically symmetric electron beam as

$$\frac{1}{r}\frac{\partial}{\partial r}\,r\,\frac{\partial \Phi}{\partial r} = \begin{cases} -\dfrac{4\pi j}{c}\left[1-\left(1-\dfrac{e\Phi}{mc^2}\right)^{-2}\right]^{-1/2}, & 0 < r \leq r_0 \\ 0, & r_0 < r \leq R \end{cases} \qquad (13.1)$$

with appropriate boundary conditions. Here, j is the current density. The radial cross section of the beam is given in Figure 13.3(a), where R is the drift tube radius and r_0 is the radius of the axially centered beam.

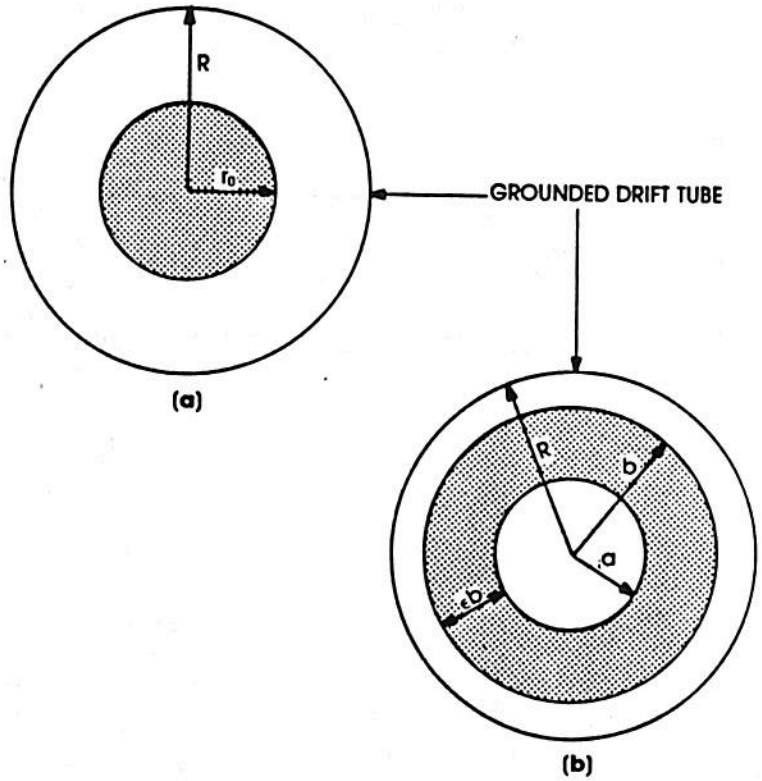

Fig. 13.3 Radial Cross Section of Two Electron Beams
Note: (a) Solid beam, where r_0 is the beam radius and R is the drift tube radius; (b) annular beam, where a is the inner radius, b is the outer radius, R is the drift tube radius, and $\epsilon = b - a/b$.

Equation (13.1) is a nonlinear differential equation. The approach taken by Bogdankevich and Rukhadze [48] is to obtain solutions by making certain analytical approximations. These approximations are related to

beam energy at injection (the nonrelativistic limit, $\gamma \approx 1$, or ultrarelativistic limit, $\gamma \gg 1$) and beam geometry (the pencil beam limit, $\ln(R/r_0) \gg 1$, or fat beam limit, $\ln(R/r_0) \ll 1$). The result is a series of first-order analytical approximations, which are restricted in validity to narrow regimes. Indeed, the most often used relation is an interpolation formula, which utilizes the uniform density approximation. The interpolation neglects the radial variations in Φ, γ, and number density n, and this formula consistently underestimates the true value of limiting current.

The work of Genoni and Proctor [50] produces a more accurate, less restricted relation for space-charge-limiting current. In particular, the relation is a second-order analytical expression, which takes into account the radial dependence of γ, Φ, and n. Also, the beam is neither confined to the ultrarelativistic limit, nor is the beam geometry valid in only certain regimes. The general electron beam radial configuration is given in Figure 13.3(b). As we can see from the figure, R is the drift tube radius, a and b are the inner and outer beam radii, respectively, and $\epsilon = b - a/b$.

The derivation also begins with conservation of energy and momentum, so that Poisson's equation for a cylindrically symmetric beam takes the form:

$$\frac{1}{r}\frac{d}{dr}\left[r\frac{d\gamma(r)}{dr}\right] = \begin{cases} \dfrac{4\nu[(b/R)^2 - (a/R)^2]}{\beta(r)}, & a \leq r \leq b \\ 0, & \text{elsewhere} \end{cases} \qquad (13.2)$$

subject to the boundary conditions:

$$\gamma(R) = \gamma_0 \qquad (13.3)$$

where $\gamma(0) \geq 1$ and finite; $\nu = Ie/mc^3$ is dimensionless current, independent of r and z. Relation (13.3) is a nonlinear differential equation, which, as expected, shows the radial dependence of γ. By choosing an appropriate Green's function, we can express (13.2) and (13.3) as an integral equation and obtain a numerical solution. More importantly, by assuming a uniform density radial profile of γ inside the beam as a *zero*th-order guess, we can iterate on the integral equation to obtain a second-order analytical approximation to the current. Thus, not only can we find the limiting current by determining the value of γ that maximizes the current, but also evaluate the current in the drift tube for any value of γ and r. By using this approach, an equivalent integral equation, valid for $a \leq r \leq b$, is

$$\gamma(r) = \gamma_0 - \frac{4\nu}{b^2 - a^2}\left[\ln\frac{R}{r}\int_a^r \frac{x}{\beta(x)}\,dx + \int_r^b \frac{x}{\beta(x)}\ln\frac{R}{r}\,dx\right] \tag{13.4}$$

A first approximation $\gamma(r) \approx \gamma^I(r)$ is obtained by putting $\beta = K$ (constant) in the integrals of (13.4). If K is fixed by requiring $\gamma^I(a) = (1 - K^2)^{-1/2}$, we obtain the following approximation to the limiting current:

$$\nu_L \approx \nu_L^{BR} \equiv \frac{(\gamma_0^{2/3} - 1)^{3/2}}{1 - f(\epsilon) + 2\ln R/b} \tag{13.5}$$

where

$$f(\epsilon) = \frac{(1 - \epsilon)^2}{1 - \epsilon/2}\left|\frac{\ln(1 - \epsilon)}{\epsilon}\right| \tag{13.6}$$

Equation (13.5), which appears in a paper by Miller and Straw [51], is the logical generalization to annular beams of the widely used Bogdankevich-Rukhadze [48] interpolation formula for solid beams, to which it reduces in the limit $\epsilon \to 1$. A second approximation, $\gamma^{II}(r)$, is obtained by repeating this procedure using $\beta = [1 - (\gamma^I)^{-2}]^{1/2}$ in the integrals of (13.4). In the special case of a solid beam ($a = 0$), the integrals can be evaluated in closed form, but they must be solved numerically for the general case of an annular beam. Genoni and Proctor [50] have obtained useful analytical approximations to $\gamma^{II}(r)$ for annular beams by performing the second iteration with $\beta = (1 - \Gamma^{-2})^{1/2}$, where $\Gamma(r)$ is a quadratic fit to $\gamma^I(r)$, which yields the exact $\gamma^{II}(r)$ in the solid beam limit. A particular choice of K then yields a definite relation between ν and $\gamma^a \equiv \gamma(a)$. The simplest of these that gives good agreement with numerical results is

$$\nu = \frac{(\gamma_0 - \gamma_a)^2}{(\Gamma_b^2 - K)^{1/2} - (\gamma_a^2 - 1)^{1/2}}\,\frac{1 - g}{(1 - f + 2\ln R/b)^2} \tag{13.7}$$

in which

$$\Gamma_b = \gamma_a + (\gamma_0 - \gamma_a)\frac{1 - g}{1 - f + 2\ln R/b} \tag{13.8}$$

and

$$g(\epsilon) = \frac{8(1 - \epsilon)^2}{\epsilon(4 - 3\epsilon)}\ln\frac{1 - \epsilon/2}{1 - \epsilon} \tag{13.9}$$

In the limit $\epsilon \to 1$, both g and f tend toward zero, and (13.7) reduces to a formula obtained by Thompson and Sloan [52, Eq. (14)] in their analysis of solid beams. The reader should note that different quadratic fits, while producing more complicated analytical expressions, produce more accurate results [50].

13.2.2 Simulation

The space-charge-flow simulations were carried out using a two-dimensional particle-in-cell plasma simulation code, CCUBE, which is fully relativistic and electromagnetic [53, 54]. CCUBE (version 1) self-consistently solves for the time-dependent trajectories of tens of thousands of plasma particles over thousands of plasma periods. The critical portion of the code consists of a "leap-frog" procedure. At each time step, the charge and current associated with the particles are interpolated bilinearly onto a spatial mesh. The quantities then serve as source terms in Maxwell's equations for determining the electromagnetic scaler and vector potentials on the mesh. Finally, the potentials are interpolated back to the particle positions. The basic coordinate system is cylindrical with the assumption of azimuthal symmetry. A uniform axially directed magnetic field can be imposed to ensure beam equilibrium.

All variables are expressed in dimensionless terms. In particular, the depth of the potential well formed by the electronic space charge is given by ϕ, where

$$\phi(r) = \frac{e\Phi(r)}{mc^2} = \gamma(r) - \gamma_0 \leq 0 \tag{13.10}$$

The five components in configuration-momentum space are $X1 = z\omega_p^0/c$, $X2 = r\omega_p^0/c$, $V1 = \gamma\beta_z$, $V2 = \gamma\beta_r$, $V3 = \gamma\beta_\theta$, where β_z, β_r, and β_θ are the components of β in the z, r, and θ directions, respectively; $\omega_p^0 = (4\pi n_o e^2/m)^{1/2}$ is the electron plasma frequency arising from the beam density at injection n_0.

In these simulations, the code is made to model the injection of cold, monoenergetic, relativistic electrons with uniform density into a long, evacuated, equipotential, cylindrical drift tube along an effectively infinite magnetic guide field in order to comply with the assumptions of Section 13.2.1. This is accomplished in the following manner.

(1.) A cold beam is obtained by setting the electron thermal velocity components equal to zero.

(2.) Miller and Straw [55] provide a criterion for neglecting the presence of end-plates, and effectively having $L \gg R$:

$$L/R \geq 2.58(b/R)^{0.133} \tag{13.11}$$

For the annular beam simulations this yields $L/R \geq 2.50$, whereas the worst-case simulation is $L/R = 9.84$. In addition, two runs were made with the downstream axial boundary grounded. The presence of end-plates did not affect the results.

(3.) Azimuthal symmetry is assured by the nature of the code.

(4.) The code injection can be made to neglect anode foil scattering so that the particles are monoenergetic and spatially uniform at injection.

(5.) Thode, *et al.* [56] give a numerical relation to ensure that the imposed magnetic field is effectively infinite. The relation is $\omega_c/\omega_p^0 \geq 5$, where ω_c is the beam cyclotron frequency defined as eB_0/mc. This condition is met by running the code's dimensionless, external, magnetic field as

$$B_0 = \omega_c/\omega_p^0 = 8.0 \tag{13.12}$$

The number of cells in the $X1$ and $X2$ direction were 190 and 37, respectively. The $X1$ length was held constant at 50.0 units to give $\Delta X1 = 0.263$ per cell. The $X2$ radius varied from 2.89 to 5.0, depending on the value of injected current. The boundary conditions for the electrons are reflection at the axis and absorption on both the radial and axial surfaces. Potentials are set to zero at the upstream axial and outer radial boundaries in order to represent metal surfaces. At the downstream axial boundary, however, the normal derivatives of the potentials are set to zero in order to simulate an infinitely long cylinder.

In Section 13.2.3, the value of γ_a from the simulation calculation is compared, for a given value of ν, with that given by (13.7), as well as with a numerical solution obtained by iterating on (13.4) with $r = a$ [50].

13.2.3 Comparison of Theory and Simulation

Several CCUBE runs were made by using $\gamma_0 = 5$ and varying values of ν in order to determine the maximum value of $|\phi|$. This consistently occurred at the radial value $r = a$. Therefore, $|\phi|$ maximizes for $\Phi(a) \equiv \Phi_a$. The characteristics of the simulation runs are given in Table 13.2. The last column in the table refers to whether the downstream axial boundary

Table 13.2 Characteristics of Simulation Runs

Run	ν	$\lvert\phi_a\rvert$	*Error* (%)	a/R	b/R	$L(c/\omega_p^0)$	$R(c/\omega_p^0)$	*Downstream Axial Boundary*
1	1.175	3.07	1.5	0	0.5	50.0	4.38	0
2	1.175	3.06	1.2	0	0.5	50.0	4.38	*G*
3	1.293	4.20	2.5	0	0.5	50.0	4.60	0
4	0.982	1.01	0.74	0.4	0.8	50.0	2.89	0
5	1.957	2.05	1.1	0.4	0.8	50.0	4.08	0
6	2.846	3.18	1.2	0.4	0.8	50.0	4.92	0
7	2.846	3.18	1.1	0.4	0.8	50.0	4.92	*G*
8	3.034	4.25	3.1	0.4	0.8	50.0	5.08	0

was grounded or open. Such a condition enabled us to check whether end-plate effects were entering the problem. As we can see in Table 13.2, no end-plate effects were noted. The percent error was derived on the basis of the code's management of conservation of energy, which is denoted by a net energy diagnostic. Because net energy continuously increases due to rounding off and truncation errors, the percent error will increase as a function of computer run time. The percent errors given in Table 13.2 were taken after the run reached a steady state, as denoted by total energy and $|\phi|$ reaching a constant, or following formation of a virtual cathode. A virtual cathode was formed in runs 3 and 8. This can be observed in the table, insofar as $|\phi_a| > (\gamma_0 - 1)$. Thus, the space-charge-limiting current lies between $\nu = 1.175$ and $\nu = 1.293$ for the solid-beam case, and $\nu = 2.846$ and $\nu = 3.034$ for the annular-beam case.

We make a comparison between the numerical, analytical, and simulation models in Table 13.3. All three methods produce consistent results for γ_a from given values of sublimiting injected current. The table lists the values given by the three methods, where

$$\gamma_a = \gamma_0 - |\phi_a| \tag{13.13}$$

is used to define γ_a for the simulations. Note that if a virtual cathode is formed, $|\phi_a| > (\gamma_0 - 1)$, then γ_a as defined by (13.13) does not have a physical meaning. Rather, it is simply a mathematical relation between γ_0 and $|\phi_a|$.

Table 13.3 Comparison of Models

ν	γ_a *Numerical*	γ_a *Analytical*	γ_a *Simulation*	*Beam Type*
1.175	1.893	1.93	1.93	Solid
1.293	Virtual Cathode	Virtual Cathode	Virtual Cathode	Solid
0.982	4.004	4.00	3.99	Annular
1.957	2.976	2.98	2.95	Annular
2.846	1.867	1.92	1.82	Annular
3.034	Virtual Cathode	Virtual Cathode	Virtual Cathode	Annular

A more important comparison can be made between the values for ace-charge-limiting current ν_L, as derived from the numerical, analytical, d simulation models, and that produced by the widely used Bogdan-vich-Rukhadze interpolation formula (13.5). This is done in Table 13.4. quation (13.5) predicts values for ν_L which are significantly lower than ose of (13.4) and (13.7). However, the analytical results differ from the sults of the integral equation by roughly 3%, and ν_L is obtained from 3.4) by numerically determining the largest value of ν for which a solution ists. The limiting current for (13.7) is derived from the value of γ_a that aximizes ν.

Table 13.4 Limiting Current Comparison

am Type	ν_L *Numerical*	ν_L *Analytical*	ν_L *Simulation*	ν_L $B - R$
lid	1.27	1.31	1.175–1.293	1.118
nular	3.03	3.12	2.846–3.034	2.712

The discrepancy in the limiting value of ν between the Bogdankevich-khadze and Genoni-Proctor formulations is due to the error involved assuming the uniform density approximation. Figure 13.4 is a plot of relation between ν and γ_a in the uniform density approximation, and a second-order analytical expression by using a better quadratic fit than .7). The simulation points have been added to the figure. It is clear t the uniform density approximation underestimates the value of ν for values of γ_a. Finally, Figure 13.5 plots $\gamma(r) - 1$ *versus* r. It shows the endence of beam kinetic energy on r for the modeled annular beam. e successively more energetic lines of dots correspond to the more recent

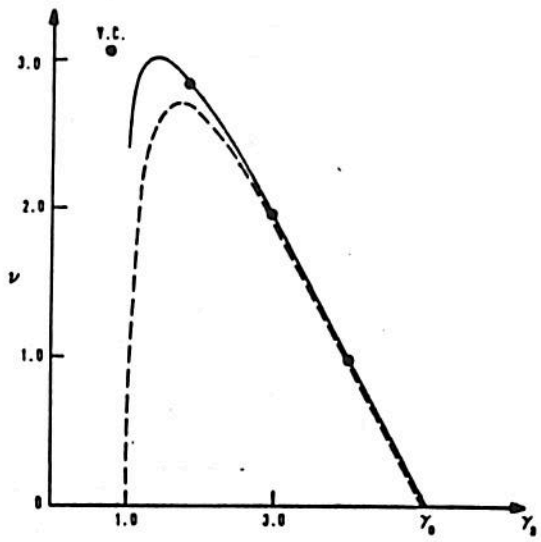

Fig. 13.4 Plot of ν *versus* γ_a for $\gamma_0 = 5$, $a/R = 0.4$, $b/R = 0.8$
Note: The dashed line represents the uniform density approximation. The solid line results from an approximate second-order analytical relation. The points correspond to simulation results. The value γ_a for the point labeled v.c. (virtual cathode) has no physical meaning. It is defined in terms of (13.13).

injections of charge through the anode. As expected, the minimum kinetic energy occurs at the inner beam edge, and the maximum occurs on the outer edge. The uniform density approximation neglects this dependence.

13.3 THE SPACE-CHARGE-LIMIT INSTABILITY

We have visualized the space-charge-limiting current as a point at which the electrostatic potential exceeds the kinetic energy of the beam. However, we may easily note from Figure 13.4 that, at the space-charge limit (SCL), the beam kinetic energy is approximately $\gamma_0^{1/3}mc^2$. Thus, although the onset of virtual cathode formation can be exactly predicted as the point at which the beam exceeds a critical current, we have only recently come to understand the dynamics of its formation and subsequent oscillations.

A small-signal perturbation analysis can be performed, just below the SCL, which seems to predict instability above the limiting current value

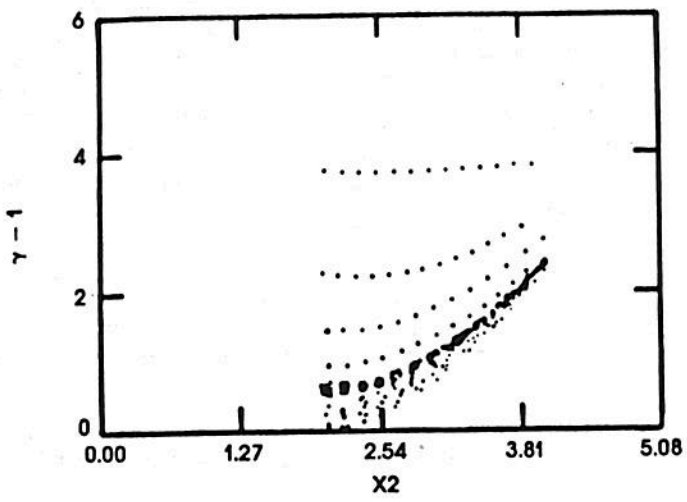

Fig. 13.5 A CCUBE Diagnostic of Particle Kinetic Energy *versus* r for the Annular Beam Showing the Radial Dependence of γ

[6, 9]. However, this analysis is not rigorous, and, in fact, produces misleading results. Instead, we can use multiple-scaling perturbation techniques to study the time-dependent behavior of a beam above the SCL. We derive estimates for the nonlinear growth rate of the ensuing instability, and show that, even below the SCL, the beam is unstable to sufficiently large perturbations. The method can be applied to a wide class of problems, but here we treat the short-circuited, one-dimensional, electrostatic diode (depicted in Figure 13.6) as the simplest model that contains the appropriate physics. We show that, at least in one dimension, an arbitrarily heavy ion background does not alter the qualitative behavior of the beam, and we present numerical results that exhibit virtual cathode oscillations for a neutral beam. Before starting this analysis, it is worthwhile for us to describe the results of numerical simulations in order to present a picture of time-dependent virtual cathode dynamics.

13.3.1 Physical Description of the Virtual Cathode

Simulations were carried out in conjunction with the theory presented in Section 13.3.2 by using a two-dimensional, relativistic, electrostatic, particle-in-cell code CCUBE (see Section 13.2.2). The code can solve self-consistently for the time-dependent trajectories of tens of thousands of plasma p[illegible]'es over thousands of plasma periods. All variables are

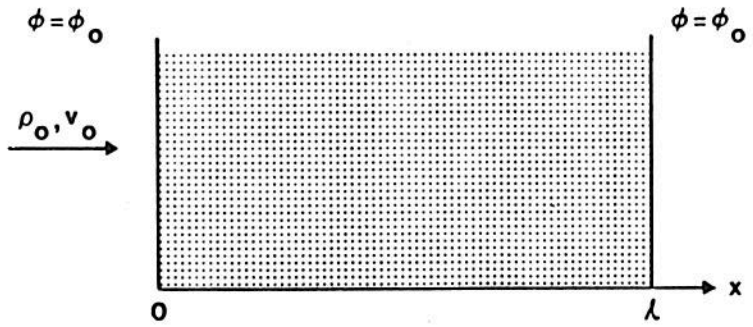

Fig. 13.6 Schematic of the Short-Circuited, One-Dimensional, Electrostatic Diode Modeled

expressed in dimensionless terms. Therefore, length is in units of c/ω_p^0, time is measured in units of $(\omega_p^0)^{-1}$, and particle velocity is given by $v_i = \beta_i\gamma (i = 1, 2, 3)$, where ω_p^0 is the initial electron plasma frequency.

In these simulations, a monoenergetic 51 keV electron beam is injected into a Cartesian geometry. The left and right boundaries are representing grounded a planar short-circuited diode. Periodic boundary conditions in the transverse direction make an effectively one-dimensional configuration space. In general, the simulation had 62 cells in the longitudinal direction, thus modeling a length of 1.0 c/ω_p^0. The time step was 0.0125 $(\omega_p^0)^{-1}$. Twenty particles were injected per cell.

A detailed discussion of the physical dynamics of the virtual cathode based on these numerical results is appropriate here. The usual graph of potential minimum ϕ_m in the diode *versus* electron beam current α is shown in Figure 13.7. (The parameter α will be discussed later.) When α is increased above the space-charge limit, ϕ_m jumps from the stable (normal-C) branch to the oscillatory stable branch. The amplitude and position of ϕ_m, while on the oscillatory branch, describe a limit cycle, as expected for a relaxation oscillation, which is what this represents. Typical limit cycles are depicted in Figure 13.8. As α is increased further the oscillation frequency ϕ_m and virtual cathode position within the diode asymptotically approach limiting values. If α is decreased, the oscillation amplitude $\Delta\phi_m$ decreases and the position of ϕ_m moves toward the diode center. The electron flow reverts to the equilibrium steady state when the perturbation, which is due to the rate of change of diode current below the space-charge limit, is sufficiently large. This normally occurs before reaching the bifurcation point. The entire process forms a hysteresis loop, which is depicted in Figure 13.7.

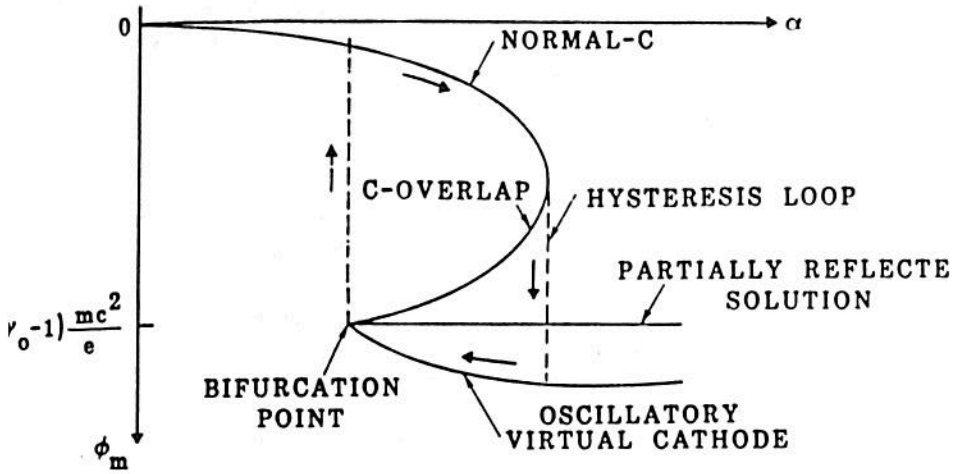

Fig. 13.7 Electrostatic Potential Minimum as a Function of Current α
Note: The plot depicts the various possible solutions such as normal-C flow (stable), C-overlap (unstable), the partially reflected solution (unstable), and the oscillatory virtual cathode (stable). The motion around the hysteresis loop is denoted by arrows.

The virtual cathode originates at the bifurcation point. This is the intersection of the oscillatory state with the C-overlap [7] and partially reflected solution branches [5]. The bifurcation point cannot be reached in the short-circuited diode. Of the three branches emanating from it, two (the steady-state ones) are physically unstable, while the oscillatory branch is numerically unstable at this point. This results because the limit cycle is infinitesimally small at the bifurcation point so that simulation codes lose resolution before they reach it. Loss of resolution creates a small-amplitude, high-frequency oscillation, observed in this study and previously [9], and this result is numerical, not physical.

The problem of loss of resolution can be overcome if we eliminate the hysteresis loop. Then, the C-overlap branch disappears, and we reach the bifurcation point along the stable normal-C branch. This can be accomplished in several ways. The most appropriate for this study is to have a retarding potential difference across the diode that is equal to the injected electron kinetic energy. Then, the C-overlap solution vanishes, and the bifurcation takes place at the space-charge limit α_{SCL}. The oscillation can be described as a small perturbation on the beam, rather than the radical change that results in the short-circuited diode when we exceed α_{SCL}. This

analysis indicates that the onset of virtual cathode formation occurs when the electron velocity in the steady state vanishes at some point inside the diode. For the short-circuited diode, this occurs at the diode center; for the biased diode, it occurs at $\leqslant l$. Because the oscillation is a small perturbation on the steady-state fields in the biased diode, the reader can readily see that the virtual cathode oscillation period at onset is the electron transit time from the injection plane to the position where velocity vanishes. This concept will be revisited in Section 13.4.

Finally, consider the particle dynamics during the oscillation period for counterclockwise limit cycles ($\alpha \leqslant \alpha_{SCL}$) as in Figure 13.8(c). At the point where the virtual cathode position is a minimum and the potential well is starting to move to the right, the amplitude is too small to stop the electrons. When virtual cathode motion is to the left, the cathode opposes the electron beam and causes particle bunching. Because the well is deeper, the stream velocity will vanish at some location, and then become negative. Here, the second derivative of the velocity (d^2u/dx^2) is also negative. In this process, the stream is continuously deformed to create a double-valued negative velocity protrusion. The entire system is three-valued (Figure 13.9), as in a collisionless shock wave [57]. Here, the region of triple flow is not limited, it is in usual collisionless shocks, by the presence of a transverse magnetic field [58], but rather the flow is limited by the presence of the walls. Indeed, the reflected part detaches from the main beam, exits periodically through the anode, and is thus responsible for the onset of oscillatory behavior in beam characteristics. As the potential minimum reaches the end of its left motion, the two "lips" of the back-reflected stream close. At this point, no more electrons are reflected and the well moves to the right, and hence repeats the cycle.

For larger values of α, the limit cycle is distorted into a figure eight, where one lobe has clockwise and the other with counterclockwise motion (Figure 13.8(b)). The transition continues until the motion is completely clockwise (Figure 13.8(a)), which indicates a change in the particle-bunching process, and this transition is related to the fraction of current that is reflected, as opposed to transmitted, from the injected electron beam. In Figure 13.8(a), most of the beam is reflected, whereas most electrons are transmitted in Figure 13.8(c).

13.3.2 Scaling Relations

Qualitative scaling relationships for the virtual cathode dynamics in one-dimensional flows can be derived from the Vlasov equation:

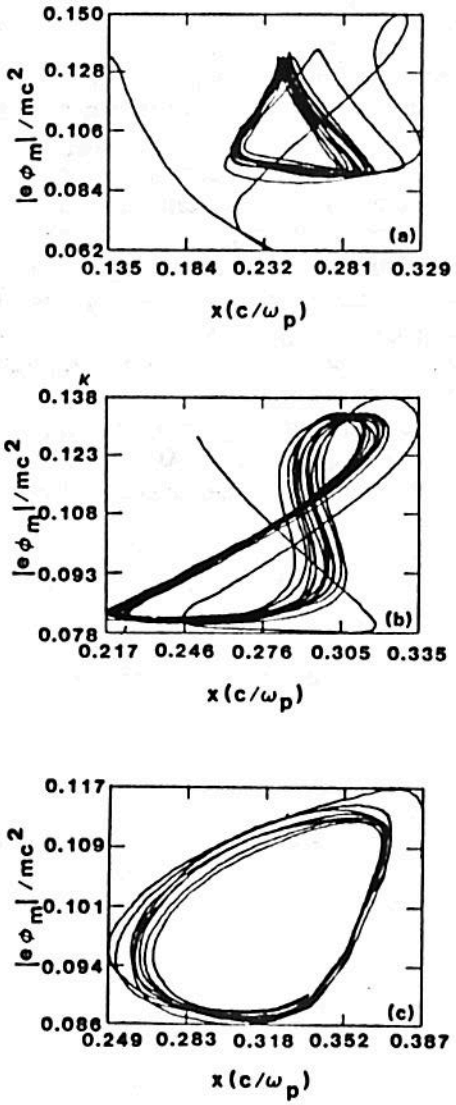

Fig. 13.8 Typical Virtual Cathode Limit Cycles in the Classical Short-Circuited, One-Dimensional Diode with an Injection Energy of 51 keV: (a) $\alpha = 2.5$; (b) $\alpha = 2.0$; (c) $\alpha = 1.4$

Note: The motion in (a) is clockwise and that in (c) is counterclockwise; $l = 1.0\ c/\omega_p^0$.

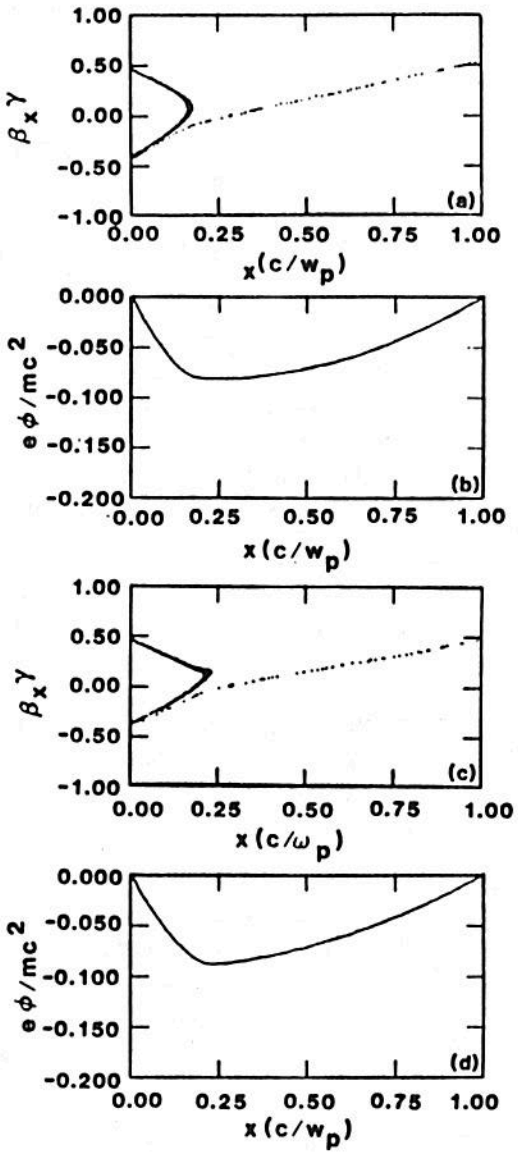

Fig. 13.9 Successive Snapshots of Electron Beam Momentum Space and Corresponding Potential Shape in the Diode for $\alpha = 2.0$, $l = 1.0\ c/\omega_p^0$

Note: The time between frames is $0.5(\omega_p^0)^{-1}$ and the initial beam kinetic energy is 51 keV.

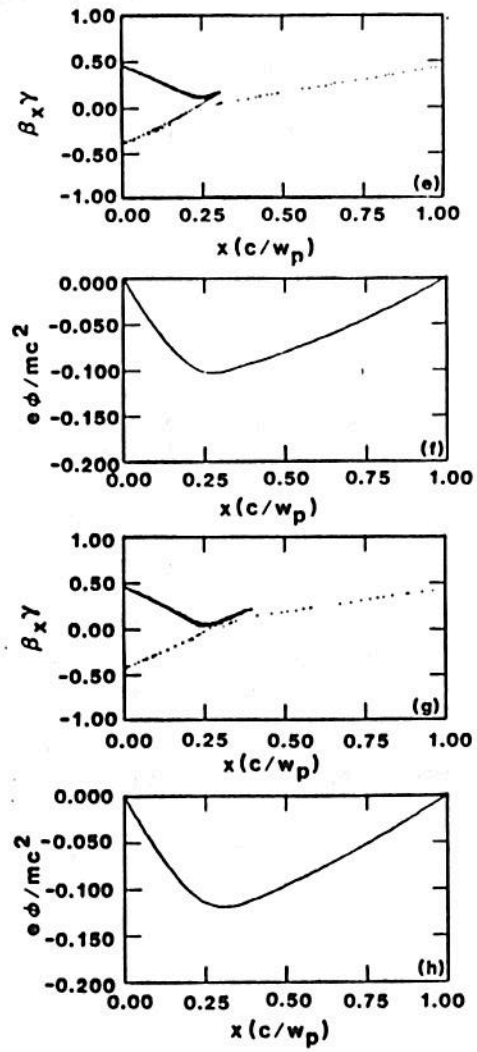

Fig. 13.9 Successive Snapshots of Electron Beam Momentum Space and Corresponding Potential Shape in the Diode for $\alpha = 2.0$, $l = 1.0\ c/\omega_p^0$

$$(\partial_t + v\partial_x + E\partial_p)f(x, p, t) = 0 \tag{13.14}$$

where x is position, t is time, p is momentum, v is velocity, and E is the

electric field. The subscripts denote derivation with respect to each variable, and f is the particle distribution function. Although the same results will follow from a fluid formulation, this approach is used to alleviate any ambiguities about their applicability to time-dependent three-velocity flows. Relativistic beams can be treated as well, if the relation between p and v is utilized, thus,

$$p = \frac{v}{(1 - v^2/c^2)^{1/2}} = \gamma v \tag{13.15}$$

Finally, we include Poisson's equation:

$$E_x = \rho \tag{13.16}$$

In order to simplify the nondimensionality, consider only cold flows with injection velocity v_0, injection momentum $p_0 = \gamma_0 v_0$, and charge density ρ_0. We will separately treat the semi-infinite and finite cases. By setting $\gamma_0 = 1$, the classical formulas can be deduced without any further analysis.

In semi-infinite geometry, the boundary conditions are given by

$$\rho(0, t) = \rho_0, f(0, p, t) = p_0\delta(p - p_0) \tag{13.17}$$

Introduce dimensionless variables $\rho = |\rho_0|n$ and $p = p_0P$ so that we have fixed boundary conditions. Next, define unknown scales for the remaining variables as $x = \xi X$, $t = \tau T$ and $E = \epsilon e$. By substituting these relations in (13.14) and (13.16), and using (13.15), we obtain

$$\left[\frac{1}{\tau}\partial_T + \frac{p_0}{\xi}\frac{P}{1 + \left(\frac{p_0}{c}\right)^2 P^2}\partial_X + \frac{\epsilon e}{p_0}\partial_P\right] \cdot F(X, P, T) = 0 \tag{13.14a}$$

and

$$\frac{\epsilon}{\xi} e_X = |\rho_0|n \tag{13.16a}$$

along with the transformed boundary conditions $n(0, t) = -1$, $P(0, t) = 1$ and $F(0, P, T) = -\delta(\hat{p} - 1)$, where $F(X, P, T)$ is the dimensionless

distribution function. If we demand $\epsilon = \xi|\rho_0|$, and we choose $\tau = \sqrt{\gamma_0/|\rho_0|}$, $\xi = v_0\sqrt{\gamma_0/|\rho_0|}$, then (13.14a) and (13.16a) become

$$\left[\partial_T + \frac{P}{\sqrt{1 + \left(\frac{p_0}{c}\right)^2 P^2}}\partial_X + e\partial_P\right] F(X, P, T) = 0 \tag{13.18}$$

$$e_X = n \tag{13.19}$$

which, together with

$$n(0, t) = -1, F(0, P, T) = -\delta(P - 1) \tag{13.20}$$

is the full dimensionless description of the problem. The only parameter still present is p_0/c. Thus, all the characteristics of semi-infinite flow are functions of only this parameter. In the classical limit, $p_0/c \to 0$, all classical flows when scaled are identical.

In finite geometry, the analysis is the same, except that if X is scaled by ξ, as noted above, the second boundary condition is given at $x = l$ by

$$X = l/\xi = \frac{l}{v_0}\left(\frac{|\rho_0|}{\gamma_0}\right)^{1/2} \tag{13.21}$$

This introduces a second parameter into the problem so that in finite geometry all characteristic quantities will be functions of

$$p_0 = \gamma_0 v_0 \tag{13.22}$$

and

$$\alpha = \frac{l\omega_p}{\beta_0\sqrt{\gamma_0 c}} \tag{13.23}$$

where ω_p is the beam plasma frequency at injection, and $\beta_0 = v_0/c$. In the classical limit, $\gamma_0 \to 1$ and $\beta_0 \to 0$, the only governing parameter is $\alpha = l\omega_p/v_0$. In the classical case, $\alpha_{SCL} = 4/3$.

13.3.3 Nonlinear Theory

A quantitative analysis of the nonlinear, one-dimensional motion of electrons in the diode is presented in [59], and is given by the equations

of continuity and momentum conservation for the electrons plus Poisson's equation. These equations are expressed here as

$$\rho_{\bar{t}} + (\rho v)_{\bar{x}} = 0 \tag{13.24a}$$

$$v_{\bar{t}} + vv_{\bar{x}} = -\frac{e}{m}\xi \tag{13.24b}$$

$$\epsilon_0 \xi_{\bar{x}} = \rho + \rho_h \tag{13.24c}$$

where $0 \leq \bar{x} \leq l$. The subscripts denote differentiation with respect to that variable. Electron and heavy ion charge density, electron velocity, electric field, time, and position are indicated by ρ, ρ_h, v, ξ, $\bar{t}$, and $\bar{x}$, respectively. The appropriate boundary conditions are $v(0, \bar{t}) = v_0$, $\rho(0, \bar{t}) = \rho_0$ and $\int \xi d\bar{x} = 0$. An ion component is placed in Poisson's equation in order to discuss two-species space-charge flow. Conservation equations of mass and momentum for the heavy ions are not included because it is assumed that their velocity does not change appreciably during their passage through the diode.

In order to simplify the mathematics, we introduce dimensionless equations for our model. These equations are

$$n_t + (nu)_x = 0 \tag{13.25a}$$

$$u_t + uu_x = -\alpha E \tag{13.25b}$$

$$E_x = \alpha(n + I) \tag{13.25c}$$

where $n = \rho/|\rho_0|$, $u = v/v_0$, $E = (e\epsilon_0/m|\rho_0|)^{1/2}\,\xi/v_0$, $t = v_0\bar{t}/l$, $\hat{x} = \bar{x}/l$, $\alpha = (e|\rho|/\epsilon_0 m)^{1/2}\,l/v_0$ is a dimensionless parameter related to current, and I is the ratio of heavy ion to electron charge densities, $I = \rho_h/|\rho_0|$. Alternatively, α may be written as $l\omega_p/v_0$, where ω_p is the beam plasma frequency. The boundary conditions for electrons become $u(0, t) = 1$, $n(0, t) = -1$, and $\int_0^1 E\,dx = 0$. For an ion beam $n(0, t) = 1$, otherwise the following derivation is the same.

Unneutralized Beams

For an unneutralized beam, by setting $I = 0$ and solving by the method of characteristics, we find

$$n^{-1} = -\frac{\alpha^2}{2}(t - s)^2 + \alpha E_0(s)(t - s) - 1 \tag{13.26}$$

where s is the entry time for the particle occupying position x at time t, and $E_0(s)$ is the electric field at $x = 0$. The particle trajectories are found by utilizing (13.25a), from which it follows that

$$\left(\frac{\partial x}{\partial s}\right)_t = n^{-1} \tag{13.27}$$

which thus yields

$$x = \frac{\alpha^2}{6}(t - s)^3 + \alpha \int_t^s E_0(s)(t - s)\, ds + (t - s) \tag{13.28}$$

Integration of the trajectory equation is hard for general time-dependent situations, because imposing the proper boundary conditions leads to a nonlinear integral equation for $E_0(t)$. However, exact solutions can be obtained for several special cases. The problem of injection into an empty diode can be integrated until the formation of a singularity in n, which indicates the crossing of trajectories. In this case, the stream velocity becomes three-valued, and we must use a Vlasov equation description [60], rather than system (13.25), which is derived assuming a single stream of monoenergetic particles. As described in Section 13.3.1, this multistreaming is characteristic of the oscillatory state created when α exceeds its SCL value.

By using these equations, we can derive a similar representation for Figure 13.7 in terms of E_0 and α. For steady states, $E_0(t) = E_0$ (constant), we find

$$u = -n^{-1} = \frac{\alpha^2}{2}(t - s)^2 - \alpha E_0(t - s) + 1 \tag{13.29a}$$

$$x = \frac{\alpha^2}{6}(t - s)^3 - \frac{\alpha}{2}E_0(t - s)^2 + (t - s) \tag{13.29b}$$

If we impose the conditions $x = 1$, $u = 1$ at $t - s = t_0$, the particle transit time, then we note that t_0 must satisfy

$$\frac{\alpha^2}{12}t_0^3 - t_0 + 1 = 0 \tag{13.30}$$

This equation has two positive solutions for $0 \leq \alpha \leq 4/3$, which coalesce at $\alpha = 4/3$. The largest one, for $0 \leq \alpha < 2\sqrt{2/3}$, does not correspond to a real flow. In Figure 13.10, we show E_0 ($= \alpha t_0/2$) *versus* α. This representation will be used in the discussion of nonlinear stability.

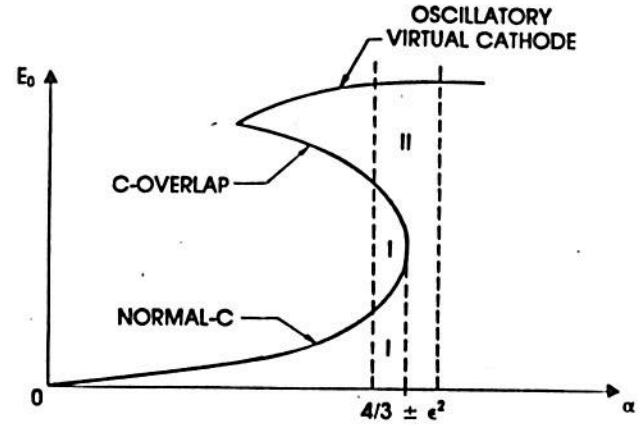

Fig. 13.10 Electric Field at the Injection Plane *versus* Current α for $I = 0$

Note: The plot depicts the normal C-flow (stable) and C-overlap (unstable) solutions. The oscillating virtual cathode (stable) solution is also shown. Regions I and II define the domains of attraction of the normal-C and virtual cathode solutions near the SCL, $\alpha = 4/3$.

Neutralized Beams

The Pierce instability occurs when electron and ion space-charge flow is considered in finite geometries, where there is no potential difference across the boundaries [61]. The ions can be either stationary or in motion with respect to electrons. Charge neutrality is maintained at the injection plane. This instability may have ramifications for charged-particle inertial confinement fusion because of its effect on neutralized beam propagation in the reactor [62]. In this section, we show that the Pierce instability is a special case of electron and ion space-charge flow. In general, two-species flow has steady and oscillatory states, which are analogous to one-species space-charge flow.

The steady-state behavior for the case of arbitrary I can be found in a manner similar to $I = 0$. By rewriting system (13.25) in characteristic coordinates, we arrive at

$$\frac{d^2}{dt^2}\left(1 + \frac{I}{n}\right) + \alpha^2 I\left(1 + \frac{I}{n}\right) = 0 \tag{13.31}$$

For positive ions ($I > 0$), the solution of (13.31), after satisfying the boundary conditions, is

$$1 + \frac{I}{n} = (1 + I)\cos\alpha\sqrt{I}(t - s) + E_0\sqrt{I}\sin\alpha\sqrt{I}(t - s) \tag{13.32}$$

Imposing conditions $x = 1$, $u = 1$ at $t - s = t_0$, we find the system:

$$1 = \frac{1}{I}t_0 - \left(\frac{1 - I}{\alpha I^{3/2}}\right)\sin\alpha\sqrt{I}\,t_0 + \frac{E_0}{\alpha I}(\cos\alpha\sqrt{I}\,t_0 - 1) \tag{13.33a}$$

$$1 = \frac{1}{I} - \frac{1 - I}{I}\cos\alpha\sqrt{I}\,t_0 - \frac{E_0}{I}\sin\alpha\sqrt{I}\,t_0 \tag{13.33b}$$

For $I = 1$, which implies charge neutralization, these equations reduce to the relations given by Godfrey [63] for the Pierce instability. However, the curves shown in Figure 13.11 are obtained by varying I. These are cuts at constant I through a three-dimensional contiguous surface. The space is defined by the axes $\tilde{E} = E_0 I^{1/2}$, $A = \alpha I^{3/2}$, and I. The surface is 2π periodic in A with the vertical plane at $A = 2\pi$ being common for all values of I. For given A, a linearized analysis establishes that the equilibria denoted by the curves are stable (unstable) for the lowest (highest) value of $\tilde{E}$. At $I = 1$, exchange of stability takes place at odd multiples of π. For $I < 1$, exchange of stability occurs at the points where $dE_0/d\alpha \to \infty$.

It is evident from Figure 13.11 that, for $I < 1$, there are no stable equilibrium solutions in the neighborhood of $A = \pi$. Therefore, we expect a virtual cathode to form when $I < 1$ and A adiabatically increases to π. We have found by using numerical simulation that in this case the beam settles to an oscillatory state similar to the virtual cathode for unneutralized beams [60]. By slowly increasing I beyond the neutral beam value of 1 in our simulation, we have established that this oscillation persists. Indeed, finding this oscillatory state for $I > 1$ by other means would have been difficult because the simulation tended to follow the stable steady branch that is r ent for all values of current.

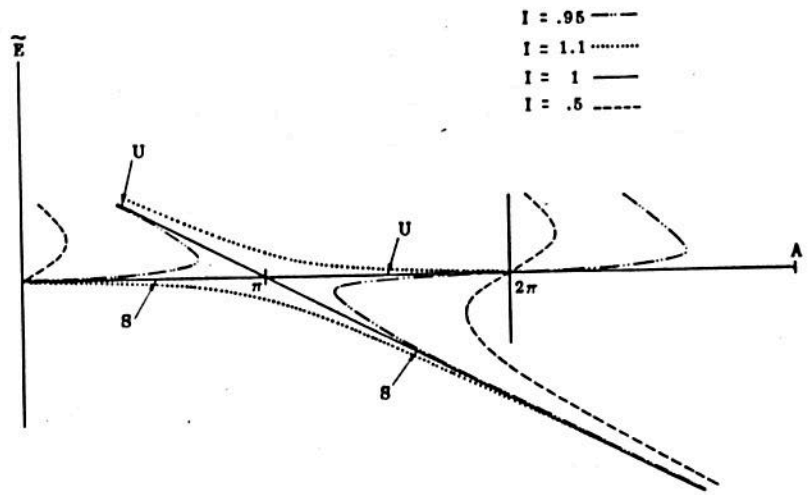

Fig. 13.11 Curves of Scaled Electric Field at the Injection Plane $\tilde{E}$ *versus* Scaled Current A for Various Values of Charge Neutralization I

Note: The curves represent slices through a three-dimensional surface. S and U respectively indicate stable and unstable branches for the $I = 1$ slice.

Nonlinear Stability Analysis

For $I < 1$, it is of interest to establish the properties of the beam instability at the SCL, generalized for $I \neq 0$ to mean the point where $d\alpha/dE_0 = 0$. We shall carry out the analysis for $I = 0$, but our method can be applied to any similar "jump" phenomenon.

A linear stability analysis [6] about the steady state described by (13.30) results in the dispersion relation:

$$(2 + \beta)\,e^{-\beta} = 2 - \beta + \frac{\beta^3}{\alpha^2 t_0^3} \tag{13.34}$$

where $\beta = i\omega t_0$. We have written the expression derived by Lomax [6] in terms of our dimensionless variables. For α near the SCL value, we let

$$\alpha = \frac{4}{3} - \epsilon^2, \quad \epsilon \ll 1. \tag{13.35}$$

and find from (13.30) that, near this value, t_0 is approximately

$$t_0 \approx \frac{3}{2} \mp \epsilon \frac{3}{2\sqrt{2}} + 0(\epsilon^2) \tag{13.36}$$

where the sign corresponds to the lower (minus) or upper (plus) branch in Figure 13.10.

By substituting in (13.34) and assuming β small, we find that

$$i\omega = \beta \approx \mp 2\sqrt{2}\,\epsilon + 0(\epsilon^2) \tag{13.37}$$

Because the linearized analysis led to time factors of the form $e^{i\omega t}$ in the perturbations, it follows that the lower branch in Figure 13.10 is stable and the upper branch is unstable, while at the SCL ($\epsilon = 0$) we have neutral stability.

Above the value $\alpha = 4/3$, linearized theory is not applicable. By utilizing multiple-scaling perturbation theory [64], we can carry out a nonlinear stability analysis near $\alpha = 4/3$. In system (13.25), we set $\alpha = 4/3 \pm \epsilon^2$. In this neighborhood, perturbations evolve on a "slow" time scale, depicted by $\tau = \epsilon t$.

If we eliminate the electric field by combining (13.25b) and (13.25c) and utilizing τ, then system (13.25) becomes

$$\epsilon n_\tau + (nu)_x = 0 \tag{13.38a}$$

$$(\epsilon u_\tau + uu_x)_x = -\left(\frac{4}{3} \pm \epsilon^2\right)^2 n \tag{13.38b}$$

where the conditions $u(0, \tau) = 1$, $n(0, \tau) = -1$, and $\int_0^1 E\,dx = 0$ are rewritten as

$$\epsilon \int_0^1 u_\tau\,dx + \frac{1}{2}[u^2(1, \tau) - u^2(0, \tau)] = 0 \tag{13.39}$$

By substituting the asymptotic expansions:

$$u \sim \sum_{i=0}^{j} \epsilon^i u_i(x, \tau) + 0(\epsilon^{j+1}), \quad n \sim \sum_{i=0}^{j} \epsilon^i n_i(x, \tau) + 0(\epsilon^{j+1}) \tag{13.40}$$

for u and n into (13.38), and equating coefficients of various powers of ϵ, a hicrachy of equations results for the u_i and n_i.

Solution of the 0(1) system gives

$$\left(u_0 - \frac{1}{2}\right)(u_0 + 1)^2 = 2(2x - 1)^2 \tag{13.41a}$$

$$n_0 = -1/u_0 \tag{13.41b}$$

To solve the $0(\epsilon)$ system, we introduce a new variable q by

$$x = \frac{16}{9}\left(\frac{q^3}{6} - \frac{3}{8}q^2\right) + q \tag{13.42}$$

so that

$$u_0 = \frac{16}{9}\left(\frac{q^2}{2} - \frac{3}{4}q\right) + 1 \tag{13.43}$$

We then find

$$n_1 = \frac{1}{u_0^2}u_1 \tag{13.44a}$$

$$u_1 = C\frac{q(q - 3/2)}{u_0} \tag{13.44b}$$

where C is a constant of integration, which is, in general, a function of the slow time τ. To find $C = C(\tau)$, which determines the slow evolution of the perturbation $u_1(x, \tau)$, we need to go to the next order, $0(\epsilon^2)$. By substituting in the expressions for u_0, u_1, n_0, n_1 and eliminating n_2, we find that $u_2(x, \tau)$ satisfies

$$(u_0u_2)_{xx} + \frac{16}{9}\frac{1}{u_0^2}u_2 = \frac{16}{9}\frac{C_\tau}{u_0}\int_0^q \frac{q(q - 3/2)}{u_0^2}\,dq + C^2\frac{q^2(q - 3/2)^2}{u_0^3} - C_\tau\left(\frac{q(q - 3/2)}{u_0}\right)_x \pm \frac{8}{3}\frac{1}{u_0} \tag{13.45a}$$

$$u_2(0, \tau) = 0, \quad u_2(1, \tau) = +\frac{9}{16}C_\tau \tag{13.45b}$$

The solution to this inhomogeneous, two-point boundary value problem exists, provided that a certain orthogonality condition is satisfied (Fredholm alternative theorem) [65] between the right-hand side and the solution of the adjoint problem that takes account of the boundary conditions. This leads to the desired equation that determines $C(\tau)$:

$$aC_\tau + bC^2 \pm c = 0 \tag{13.46}$$

where a, b, and c are found to be

$$a = -\int_0^{3/2} \frac{q(q - 3/2)}{u_0^2}\left[\frac{16}{27}q^2(q - 9/4) + \frac{3}{2}\right] dq = 1.6850 \tag{13.47a}$$

$$b = \frac{8}{3}\int_0^{3/2} \frac{q^3(q - 3/2)^3}{u_0^4}\, dq = -3.7968 \tag{13.47b}$$

$$c = \frac{8}{3}\int_0^{3/2} q(q - 3/2)\, dq = -1.5 \tag{13.47c}$$

In (13.46) the plus or minus signs indicate that we are above or below the SCL, respectively.

Above the SCL, we find

$$C(\tau) = -\frac{c}{b}\tan\left[\sqrt{cb}\left(\frac{\tau + \tau_0}{a}\right)\right] \tag{13.48}$$

and below the SCL, we have

$$C(\tau) = \frac{c}{b}\tanh\left[\sqrt{cb}\left(\frac{\tau + \tau_0}{a}\right)\right], \quad \text{if } |C(0)| < \sqrt{c/b} \tag{13.49}$$

$$C(\tau) = \frac{c}{b}\coth\left[\sqrt{cb}\left(\frac{\tau + \tau_0}{a}\right)\right], \quad \text{if } |C(0)| > \sqrt{c/b} \tag{13.50}$$

where τ_0 is a constant of integration. In general, small initial perturbations will lead to the solution:

$$u(x, t) \sim u_0 + \sum_{i=1}^{I} C_i(\tau)\, e^{\omega_i t} u_i(x) + 0(\epsilon^2) \tag{13.51}$$

where ω_i are the various distinct solutions of the dispersion relation (13.14) at $\alpha = 4/3$ [64, 66]. It is straightforward to show that all modes are such that $\mathrm{Re}(\omega_i) < 0$, except one for which $\omega = 0$. Thus, all other modes will decay in the fast time scale, and only the neutral mode ($\omega = 0$) will persist. Our solution after a short time will look like so

$$u \sim u_0 + \epsilon C(\tau)\frac{q(q - 3/2)}{u_0} + 0(\epsilon^2) \tag{13.52}$$

From the given initial conditions, it is easy to determine the initial condition for the neutral mode. Below the SCL, if the initial conditions are such that $C(0) > -\sqrt{c/b}$, the solution will evolve to the stable lower branch in Figure 13.10 (region I), while if $C(0) < -\sqrt{c/b}$, $C \to \infty$ in finite time (Figure 13.10, region II). A blow-up in finite time also occurs above the SCL for any $C(0)$. This does not mean that the actual solution blows up, just that it evolves to a final state far away from the two steady branches shown in Figure 13.10, and thus is not accessible by using perturbation theory.

As we can see in (13.48), the blow-up above the SCL is described by a tangent function, and therefore we must appropriately interpret the growth rate that we find for this case. Note that the linearized dispersion relation seems to suggest an imaginary exponential growth rate above the space-charge limit [3, 6]. In view of our results, we see that this is actually misleading; moreover, we find that, even below the SCL, the stable steady branch can be destabilized by sufficiently large perturbations.

Our results agree with the linear theory, provided that we consider the limit where the latter becomes applicable. Thus, we must compare the linear theory with (13.49) as $\tau \to +\infty$ (near the stable branch) and (13.50) as $\tau \to -\infty$ (near the unstable branch). To demonstrate this, we set $\tau = \epsilon t$ in (13.49), and consider the limit $t \to +\infty$. Then,

$$C(t) = \frac{c}{b}\tanh\left[\frac{\sqrt{cb}}{a}(\epsilon t + \tau_0)\right]$$

$$= \frac{c}{b}\left\{\frac{1 - \exp - \left[\dfrac{2\sqrt{cb}}{a}(\epsilon t + \tau_0)\right]}{1 + \exp - \left[\dfrac{2\sqrt{cb}}{a}(\epsilon t + \tau_0)\right]}\right\}$$

$$\approx \frac{c}{b}\left\{1 - 2\exp - \left[\frac{2\sqrt{cb}}{a}(\epsilon t + \tau_0)\right] + \ldots\right\} \tag{13.53}$$

We see that the decay rate of the perturbations as $t \to +\infty$ is equal to

$$\frac{2\sqrt{cb}}{a}\epsilon \approx 2.83\epsilon \tag{13.54}$$

which is the same as that found by the linearized analysis [6]. This quantity is important because it also determines an initial *growth rate* for the jump instability above the SCL described by (13.48). If we substitute the original dimensional time variable into our expressions and write the deviation of α from its value at the SCL as

$$\epsilon = (\alpha - \alpha_{SCL})^{1/2} = \left(\alpha - \frac{4}{3}\right)^{1/2} \tag{13.55}$$

we find that the growth rate is given by

$$D = \left(\alpha - \frac{4}{3}\right)^{1/2}\frac{\sqrt{cb}}{a}\frac{v_0}{l} \tag{13.56}$$

or

$$D = \left(\frac{l\omega_p}{v_0} - \frac{4}{3}\right)^{1/2}\sqrt{2}\,\frac{v_0}{l} \tag{13.57}$$

Of course, for the expansions in (13.51) to be valid, we must have $C(\tau) \ll 1/\epsilon$. However, when C is not too large, (13.48) gives a reliable estimate for the growth rate of the instability.

13.4 A LINEAR THEORY OF VIRCATORS

In the previous sections, the virtual cathode and space-charge-limit instability have been modeled as one-dimensional electrostatic phenomena. The linear theory presented in this section addresses electromagnetic effects, which give rise to the generation of microwaves. Microwave tubes can be broadly divided into devices where an electron beam interacts with

the electromagnetic fields in a "gap," and devices where the beam interacts with a traveling wave. In some devices, the division can become blurred, but the vircator is rather clearly a member of the first group.

The basic vircator configuration is shown in Figure 13.12(a). Two resonator sections, l_1 and l_2, are separated by a screen mesh, which also serves as an anode (A) for an electron beam formed at the cathode (K). A schematic view of the (zero-order) kinetic energy (ϵ_e) of a typical electron is also shown in Figure 13.12(b). The electron is accelerated across the first A-K gap, and passes through the mesh anode into the second resonator. If the beam current density is above the space-charge limit, a virtual cathode will be formed in the second resonator and the beam will reflex.

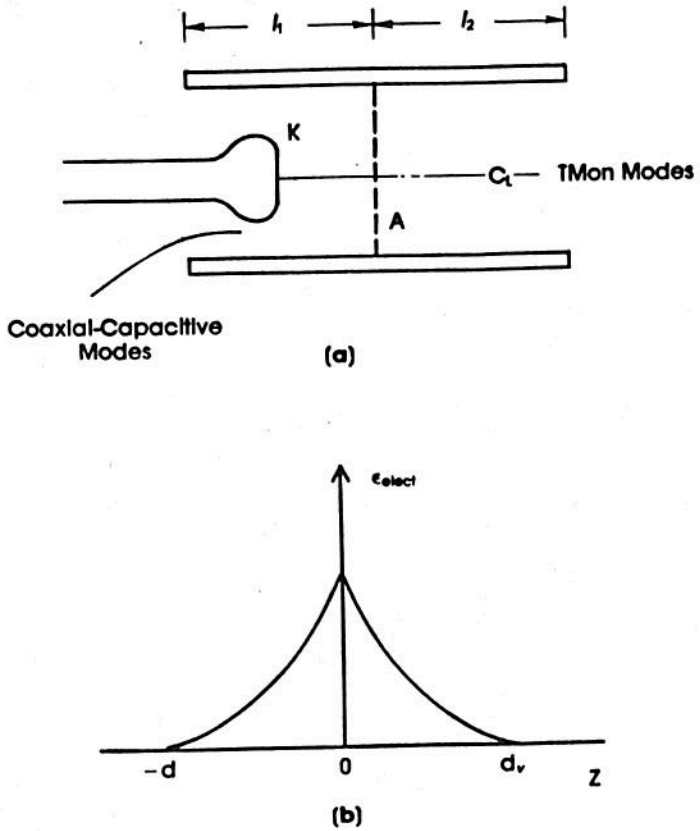

Fig. 13.12 (a) Basic Vircator Configuration and (b) Electron Beam Energy Profile

13.4.1 Vircator Operating Modes

It is possible to identify two general operating modes and a variety of subclasses. In the first, which may be called a *simple vircator*, the A-K gap provides the electron beam, but plays no other role in generating radiation. The screen mesh is assumed as opaque to microwaves, and the properties of the system depend on the resonator l_2 and the electron-beam–virtual-cathode configuration. Oscillating fields in resonator l_2 will first modulate in velocity and then bunch the electron beam. Microwave energy can be extracted, given the proper phase relation between the bunched electrons and the fields. This single (A-K_v) gap system might be expected to resemble a monotron in its operation, and the analogy will be further examined below.

The second basic mode resembles a klystron. In this case, the screen still remains opaque to microwaves, but the properties of resonator l_1 are such that some velocity modulation occurs in the first (A-K) gap. The beam reflexes in the A-K_v region with an associated conversion of velocity modulation to density modulation. Again, when the proper relations are maintained, the returning bunched beam drives the oscillation on the real A-K gap. The analogy to the klystron will also be further explored below.

Both types of devices have been modeled numerically, and they are viable means of producing high-power radiation. Both modes have been observed experimentally as well. In some experiments, blocking the reflexing current, which occurs predominantly on the beam axis, where the virtual cathode potential is a minimum, drastically reduces the microwave signal [33]. In other experiments, the microwave generation is observed to be much greater from the virtual (A-K_v) diode than the real (A-K) diode [36]. In general, a mixture of both modes is present.

The operating mode that dominates depends on which feedback mechanism is most important for a given experimental configuration. This is related to the proportion of beam current, which is reflected by the virtual cathode. If the reflected current is large, the presence of the reflected space charge in the A-K gap forces the diode to operate with a time-dependent impedance, the period of which is determined by the virtual cathode oscillation. Thus, the electrons emitted from the cathode are strongly modulated before they enter the A-K_v gap. Preventing this feedback in the real diode lowers the efficiency of microwave generation. If the reflected current is small, the feedback to the virtual cathode must be supplied by the configuration of resonator l_2. The resonator need not be a true cavity. Impedance mismatches in the waveguide interact with free space, or an antenna may supply sufficient feedback. The larger is the impedance mismatch, then the stronger is the feedback to the virtual cathode, which results in greater beam modulation.

The amount of reflected current is determined by the ratio of the injected beam current to the space-charge-limiting current (I/I_{SCL}). The higher is the ratio, then the more important the reflexing mechanism becomes to the generation of microwaves. Indeed, the nature of the virtual cathode oscillation changes as the I/I_{SCL} increases. We can see this in the virtual cathode limit cycles, depicted by Figure 13.13. Near the space-charge limit, a well defined virtual cathode exists, which repeats its periodic cycle. Well above the space-charge limit, the cycle reverses direction. Rather than the original potential minimum repeating its motion by moving back toward the injection plane, a second virtual cathode is formed near the anode. Because the virtual cathode loses its "memory" in this case, a beam premodulated which enters the A-K_v gap will be more efficient in generating microwaves, if other feedback mechanisms are not present.

In addition to the options described here, many other possible variations exist. The screen mesh will generally not be completely opaque to microwave radiation, and hence resonators l_1 and l_2 will couple. Among the many possibilities thus created, one highly nonlinear variation deserves specific mention. If fields in resonator l_2 create a certain amount of first velocity modulation, then density modulation, then the drive coupled into the real A-K gap may further modulate the incoming beam. Once again, assuming a favorable accumulation of phase relations, the end state would be a highly modulated beam that is driving the fields of resonator l_2. In this limit, a considerable fraction of the incoming beam energy may be converted to radiation. In some respects, this option resembles a two-cavity klystron.

13.4.2 Small-Signal Theory

In order to assess quantitatively the concepts introduced in the preceding subsection, we must further consider the interaction of an electron beam with the fields in a gap. This will be done in two steps: first, we will evaluate the energy exchanged in the small-signal limit; subsequently, we will deduce an expression for the beam-related gap admittance.

If an electron beam enters a gap across which there is a spatially uniform oscillating voltage, the beam will first velocity modulate, then, if the gap is long enough, density modulate (Figure 13.14). The energy exchange may be computed from

$$\frac{d\epsilon}{dt} = \frac{1}{2}\,\mathrm{Re}\int_{\text{beam}} \mathbf{J}^* \cdot \mathbf{E}\, dV \tag{13.58}$$

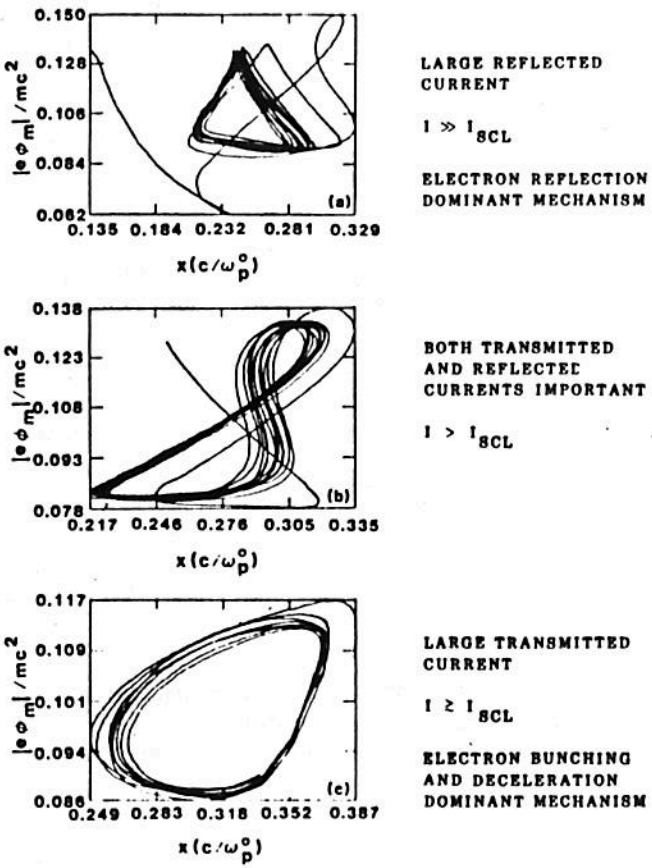

Fig. 13.13 Ratio of Beam Current to Space-Charge-Limiting Current Determines Whether Electron Reflexing or Bunching is the Dominant Microwave Generation Mechanism

where $\mathbf{J}^*$ is the complex conjugate of the current modulation produced by the gap field $\mathbf{E}$, and the integration is over the volume of the beam in the gap. The rate of energy exchange may be conveniently scaled in units of the energy stored in the resonator ϵ_s and the angular frequency ω of the oscillating field. We define

$$\frac{1}{Q} \equiv -\frac{1}{\omega \epsilon_s}\frac{d\epsilon}{dt} \tag{13.59}$$

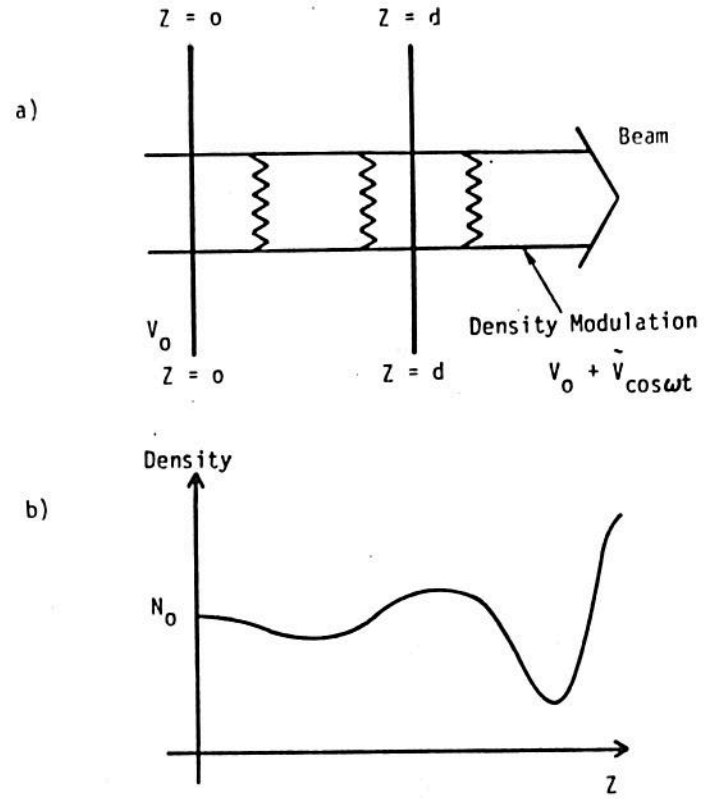

Fig. 13.14 (a) Electron Beam-Gap Configuration and (b) Beam Density Profile as a Function of Distance

The threshold for oscillation:

$$\frac{1}{Q_b} < 0 \text{ and } |Q_b| < Q_L \tag{13.60}$$

where Q_b and Q_L are the beam and loaded-cavity quality factors. The oscillation threshold may be computed with aid of the solution of the equations governing the electron dynamics.

Also useful is the definition of a beam admittance Y_b in terms of the energy exchange rate and the oscillating voltage $\tilde{V}$ on the gap:

$$\text{Re } Y_b = -\frac{1}{|\hat{V}|^2}\frac{d\epsilon}{dt} \tag{13.61}$$

The complete admittance is determined from

$$Y_b = G_b + iB_b = \int_V \mathbf{J}^* \cdot \mathbf{E}\, dV \tag{13.62}$$

Thus, it is possible to characterize the beam-gap interaction in terms of an equivalent circuit, which consists of Y_b in parallel with the equivalent circuit of a cavity resonator. Threshold is now alternatively defined as

$$\text{Re } Y_b > \frac{1}{R_L} \tag{13.63}$$

where R_L is the equivalent total (cavity plus useful load) resistance. Furthermore, when the oscillation may be treated as approximately steady state, there is also a dynamic frequency shift, defined by

$$B_b = \omega C - \frac{1}{\omega L} \tag{13.64}$$

which will vanish only on resonance.

In the small-signal limit, it is a straightforward matter to evaluate $1/Q_b$. If we define the perturbation on the electron momentum distribution function δf, we obtain the following expression:

$$j = -n_0 e \int dp\, \delta f \mathbf{v} \tag{13.65}$$

(n_0 = average density of the incoming beam). The Vlasov equation may be used to obtain an expression for δf. Then, with the aid of a series of steps, which need not be evaluated in detail here, we obtain the expression:

$$\frac{1}{Q_b} = \frac{\nu}{2(\beta\gamma)^3}\frac{d^3|E|^2}{\epsilon_g(1 + \epsilon_{ext}/\epsilon_g)}\,\text{Re}\,\Gamma'(\theta) \tag{13.66}$$

The parameters not yet identified are

d = gap length;
ϵ_g = energy stored in the gap;
E = oscillating electric field in the gap;
ϵ_{ext} = energy stored in the resonator volume, which is external to the gap.

Also,

$$\text{Re}\,\Gamma'(\theta) = \frac{2(1 - \cos\theta) - \theta\sin\theta}{\theta^3} \tag{13.67a}$$

where

$$\theta = \omega\tau_0 = \frac{\omega d}{v_0} \tag{13.67b}$$

The two expressions (13.67) describe the dependence of the gain (and the form of Y_b) in terms of the undisturbed transit angle θ (τ_0 is the time that an electron, which is undisturbed by the oscillating field, takes to cross the gap). Note that θ has the same form as α discussed in Section 13.3. Equation (13.67) is sketched in Figure 13.15.

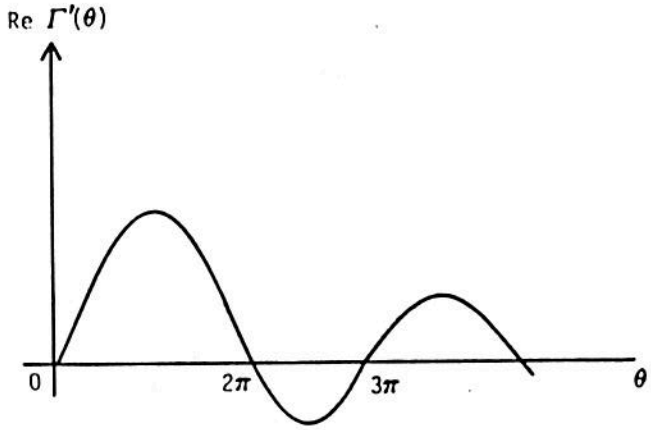

Fig. 13.15 The Function Re $\Gamma'(\theta)$

The Vircator-Monotron

When the transit angle is increased, the function $\Gamma'(\theta)$ has regions where it is negative, and hence instability becomes possible if $1/|Q_b| > 1/Q_L$. The peak gain (max $1/|Q_b|$) occurs near

$$\omega\tau \approx 2\pi(n + 1/4) \tag{13.68}$$

Hence, if τ is known, we can compute the frequency of the radiation produced in this single-gap system.

If the beam is not subjected to an accelerating field in the gap (a drifting beam), then (13.68) predicts

$$f = \frac{(n + 1/4)v_0}{d} = 30(n + 1/4)\frac{\beta_0}{d} \quad \text{(GHz)} \tag{13.69}$$

An essentially similar result is obtained when a constant accelerating field is present across the gap. The factor of 30, however, becomes 15 in this limit because the average velocity determines τ. This class of instability, usually termed the *monotron oscillator*, will also show a $V^{1/2}/d$ dependence of the operating frequency, as has been seen experimentally [22] and in PIC code simulations for the vircator [67]. If a system with a virtual A-K_v gap were undergoing a monotron type of oscillation, the transit time would be determined by the zero-order electron dynamics, and it would be generally expected to scale as $j_0^{1/2}$ (j_0 the zero-order current density). Equations (13.61) and (13.66) may be used to obtain τ in the nonrelativistic limit, $\gamma \to 1$; thus,

$$\text{Re } Y_b = \frac{I}{2V_0}\theta\Gamma'(\theta) \tag{13.70}$$

The result summarized in (13.70) is very simple. The gap admittance is proportional to the zero-order beam admittance. In a conventional microwave tube, this quantity is low, and the implied high threshold generally relegates the monotron to the class of devices that are theoretically interesting, but unimportant in practice. The low admittance also generally means that the saturation amplitude will be low, and this is a further objection to practical monotrons if they are based on conventional microwave tube technology. When low-impedance generators are employed, however, not all of these conclusions apply.

The Vircator-Klystron

In the introduction, we described a vircator-klystron mode, and for better understanding of this possibility, a few remarks about the conventional reflex klystron will be of use. The latter device has a single cavity, which first provides velocity modulation, and the condition $\omega\tau_0 \ll 1$ usually applies in this gap. The beam leaves the modulating gap, then moves into a retarding field region and begins to bunch. The various potentials are arranged so that the bunch arrives back at the gap during the maximum retarding phase of the oscillating voltage, and energy is extracted from the beam.

The small-signal admittance of this system may be described by

$$Y_b(\theta) \approx \frac{I}{V_0}\theta e^{i(\pi/2-\theta)} \tag{13.71}$$

where θ is again a transit angle. Note that $Y_b(\theta)$ in (13.71) is approximately θ^3 larger than the monotron admittance. Furthermore, θ itself can now be large because it is associated with a decelerating region and not a gap transit angle.

The angle θ where maximum gain occurs is given by

$$\theta = 2\pi(n - 1/4) \tag{13.72}$$

and this gain will increase with n (lower threshold). In the conventional klystron, the magnitude of the transit angle is controlled by the size of the retarding voltage, while in a vircator-klystron, this potential will be equal to the cathode voltage. Hence, a vircator-klystron might be expected to operate in an $n = 1$ mode. Due to the high threshold current required, conventional reflex klystrons do not generally make use of the lowest order mode.

For operation in the $n = 1$ mode, however, the operating frequency will be

$$f = \frac{3}{4}\frac{1}{\tau} \approx \frac{1}{2}\sqrt{\frac{eV_0}{md^2}} \tag{13.73}$$

which is nonrelativistic, where the last relation follows from the Child-Langmuir law. Again, the frequency depends on the real gap, but the frequency will be lower [15 $(n - 1/4)\,\beta_0/d$ (GHz)].

13.4.3 Evaluation of the Vircator Frequency with Maximum Gain

Based on this linear theory and the virtual cathode scaling laws derived earlier, we may now evaluate the vircator frequency at which we can obtain maximum gain. The scaling laws (Section 13.3.2) indicate that the vircator's fundamental oscillation frequency is related to the relativistic beam plasma frequency, given by

$$\omega_p^{rel} = \left(\frac{4\pi n_0 e^2}{\gamma m}\right)^{1/2} \tag{13.74}$$

For a nonrelativistic beam in a semi-infinite, one-dimensional drift space, the vircator frequency ω_{osc} is directly proportional to the beam plasma frequency, given by (13.74) with $\gamma = 1$. This is a good approximation for most nonresonant vircator experiments being conducted to date because the beam is of low energy, and the drift tube length is significantly greater than its radius. Therefore, $\omega_{osc} \propto n_0^{1/2}$. The current density extracted from a planar diode is defined by the nonrelativistic Child-Langmuir relation, which is

$$j_{CL} = \frac{4}{9}\left(\frac{2e}{m}\right)^{1/2}\frac{V_0^{3/2}}{4\pi d^2} = n_0 e v_0 \quad = 2.34\,\frac{V_0^{3/2}}{d^2}\ \text{KA/cm}^2 \tag{13.75}$$

(V_0 (MV), d (cm))

where V_0 is the diode voltage, d is the anode-cathode (A-K) gap spacing, and v_0 is the electron velocity at injection. An expression for velocity is obtained from conservation of energy. It is

$$v = \left(\frac{2e}{m}\right)^{1/2} V^{1/2} \tag{13.76}$$

Note that we have consistently ignored relativistic effects in ω_{osc}, j_{CL}, and v_0 in this derivation. If we combine (13.75) and (13.76), and solve for n_0, then we obtain

$$n_0 = \frac{1}{9\pi e}\frac{V_0}{d^2} \tag{13.77}$$

or

$$\omega_{osc} \propto \omega_p = \frac{2}{3}\left(\frac{e}{m}\frac{V_0}{d^2}\right)^{1/2} \tag{13.78}$$

Thus, $\omega_{osc} \propto (V/d^2)^{1/2}$. This is precisely the dependence seen in planar-diode vircator experiments to date [22, 25].

We can now include the linear theory. Note that (13.69) and (13.73) assume one-way, unperturbed (i.e., small-signal) transit times across the gap, as given by d/v_0, where v_0 is the initial velocity of the electron, which are equal to $(2eV_0/m)^{1/2}$. These equations predict frequencies that are high for the vircator in comparison with simulation results [67]. This is because the vircator oscillation frequency depends on the two-way transit time across the A-K_v gap. That is, the periodicity of the electrons is from the anode to virtual cathode and back again. When combined with the strong electric field, which the electrons observe over one cycle, first retarding, then accelerating, this implies that $\tau = 4\tau_0$. By using (13.72) with $\theta = \omega\tau = 4\omega\tau_0$, $\tau_0 = d/v_0$, $v_0 = (2eV_0/m)^{1/2}$, and setting $n = 1$, we obtain

$$\omega_{osc} = \frac{\pi}{2}\cdot\frac{3}{4}\cdot\left(\frac{2eV_0}{md^2}\right)^{1/2} \tag{13.79}$$

A comparison of (13.78) with (13.79) yields

$$\omega_{osc} = \frac{\pi}{2}\cdot\frac{3}{4}\cdot\frac{3\sqrt{2}}{2}\,\omega_p = \frac{5}{2}\,\omega_p \tag{13.80}$$

which is precisely the result seen experimentally in our work [45] as well as from nonlinear one-dimensional electrostatic [60] and two-dimensional electromagnetic [26, 67] simulations at both nonrelativistic and relativistic voltages. This appears to indicate that the simple vircator indeed works like a reflex klystron with $n = 1$ and $\tau_0/\tau \sim 0.25 \ll 1$, rather than as a monotron.

It is important for the reader to note that, while maximum gain occurs at 5/2 ω_p^{rel}, the bandwidth of the vircator over which gain occurs is large. Thus, waves at frequencies other than 5/2 ω_p^{rel} may grow if the vircator configuration allows feedback at those frequencies. Such is the case when the virtual cathode is surrounded by a cavity. The cavity supplies strong feedback at its modes, which results in the vircator frequency shifting away from maximum gain, or microwave growth at multiple frequencies, unless there is proper tuning of the cavity.

13.4.4 Signal Efficiency

If space-charge forces due to bunching are neglected (a questionable assumption if the bunching efficiency is high), it is a straightforward matter

to determine also the dependence of Y on the oscillating voltage. In general terms, as V increases, the magnitude of Y drops, and this roll-off determines the *steady-state operating point*:

$$\text{Re } Y \approx \frac{J_1(X)}{X} \tag{13.81a}$$

where J_1 is a Bessel function of first order, and X is the bunching parameter:

$$X \approx \frac{e\hat{V}}{V_0} \tag{13.81b}$$

Following the klystron analogy, $\theta = 3\pi/4$ for a vircator-klystron, and in this limit the peak efficiency could reach

$$\eta \approx \frac{1.25}{\theta}$$

or about 53%. We do not expect that this peak efficiency could be immediately achieved in practice, but it indicates the potential advantage to be gained from a detailed understanding of the relevant impedances and how they relate to beam-field coupling.

13.5 MICROWAVE GENERATION FROM THE NONRESONANT VIRCATOR

Before we consider microwave generation from the nonresonant vircator, it is useful to summarize the results from the earlier sections. The virtual cathode oscillator occurs when the beam current injected into a waveguide or cavity resonator exceeds the space-charge-limiting current. The limiting current is defined by the beam energy and the waveguide or resonator geometry. We can visualize simplistically the space-charge-limiting current as that at which the electrostatic potential exceeds the kinetic energy of the beam. Above the space-charge limit, no stable steady state for the electron beam exists. Instead, the beam experiences a jump instability, whereby it transits from a stable steady state to an oscillatory, but nonetheless stable, equilibrium. This oscillatory state is the virtual cathode. The space-charge-limiting current for a solid beam in vacuum, in cylindrical geometry, is given approximately by the following interpolation formula [48] (for more accurate formulas, see Section 13.2.1):

$$I_{SCL} = \frac{mc^3}{e}\frac{(\gamma^{2/3} - 1)^{3/2}}{1 + 2\ln R/r_0} \quad (mc^3/e = 17 \text{ kA}) \tag{13.82}$$

where γ is the beam relativistic factor at the anode (γ = 1 + voltage (kV)/511), R is the radius of the waveguide or cavity, r_0 is the electron beam radius, c is the speed of light, and e and m are the electronic charge and rest mass, respectively.

The virtual cathode oscillates stably at a set frequency in both time and space. This fluctuating potential barrier acts as a gate to reflect some electrons and transmit others. The motion of the gate causes charge to bunch. The charge bunch and virtual cathode are spatially separated as shown in Figure 13.16. By analogy, this configuration represents an LC oscillator. The virtual cathode acts as a capacitor to store the beam kinetic energy. During that portion of the cycle in which the potential is greater than the injected beam energy, charge is constrained to remain near the anode. This starves the virtual cathode so that its amplitude decreases below $(\gamma_0 - 1)\, mc^2/e$. Some of the charge bunch is transmitted once this occurs. The electron motion represents a large, time-varying current through an inductor. The presence of charge away from the anode reestablishes the virtual cathode, and the cycle repeats. The oscillating current generates microwaves. The wave frequency is that for oscillation of the virtual cathode. Maximum growth occurs at 5/2 ω_p^{rel}. This result can be rewritten for planar diodes by using the Child-Langmuir law, as

$$f(\text{GHz}) = 10.2\sqrt{j(\text{kA/cm}^2)/\beta\gamma} \tag{13.83}$$

A large number of the vircator experiments to date have been conducted in a geometry where the electron beam is injected into a long waveguide [22, 24, 25, 31, 33, 35, 36, 68]. The microwaves are diagnosed either in the waveguide terminated by a calorimeter [31, 68], or in open air after extraction [22, 24, 25, 33, 35, 36]. In either case, there is usually insufficient feedback to shift the vircator frequency from that predicted for maximum gain. These experiments are generally characterized by broad-bandwidth microwave generation, which usually excites the waveguide mode closest to cut-off. These characteristics will now be examined.

13.5.1 Vircator Waveguide Mode

The vircator's choice of waveguide mode is evident in simulations where there is no axial magnetic field. If a cold beam is injected and azimuthal symmetry is assumed, the only nonzero fields are E_z, E_r, and

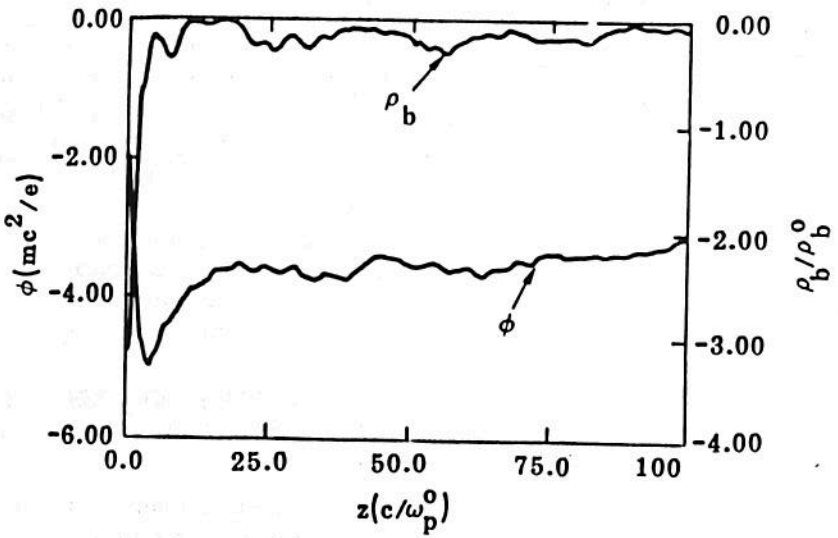

Fig. 13.16 CCUBE Diagnostic of Charge Density ρ_b and Potential ϕ as a Function of a Longitudinal Distance z for an Electron Beam in a Two-Dimensional Drift Space with an Imposed (Large) Axial Magnetic Field

Note: ρ_b is normalized to its value at injection. The value of $(\gamma_0 - 1)$ is 4. The minimum charge density and potential are separated in z.

B_θ in cylindrical geometry. These three fields define a transverse magnetic or TM wave. The direction of wave propagation is, of course, determined by the Poynting flux $(\vec{E} \times \vec{B})$. In this case, there will be both axial and radial components of the wave vector $\vec{k}$. This explains why both polarizations are observed in axially extracted vircator experiments [33, 35]. The wave vector in this case is given by

$$\vec{k} = \frac{|E_r|}{|E|}\hat{k}_z + \frac{|E_z|}{|E|}\hat{k}_r \tag{13.84}$$

Because the latter term dominates, the Poynting vector is predominantly directed radially outward. The phase velocity of the wave can be expressed as

$$\frac{v_p}{c}\sqrt{1 + \tan^2\Psi} = \sqrt{1 + \left(\frac{k_r}{k_z}\right)^2} \tag{13.85}$$

where Ψ is the angle between the $\vec{k}$ vector and the z-axis. Because E_z is usually substantially greater than E_r, the vircator preferentially excites the mode closest to cut-off, where the phase velocity can be much greater than c. This does not preclude excitation of lower order TM_{0n} modes. This is particularly true, if the beam cross section overlays a particular node of the J_0 Bessel function upon injection into the waveguide. Note that, whereas in axially extracted vircators a symmetrically configured diode excites a TM_{0n} mode, in radially extracted vircators the output mode will be TE_{1n}.

13.5.2 Vircator Bandwidth

In the absence of a resonant structure, the vircator bandwidth tends to be large due to three factors. These are *nonuniform voltage, A-K gap closure,* and *beam temperature.* This can be understood by examination of (13.78). The dependence of vircator frequency on voltage explains the importance of a flat-top voltage pulse in producing a narrow bandwidth. The closure of the A-K gap, which is due to plasma motion inherent in any foil system, will make the frequency increase during the pulse length as d decreases. This is an effect witnessed in vircator experiments with no resonant cavity [33, 35, 36, 45]. This also makes the spectrum appear broader. An expression for these observations, which is obtained by differentiating (13.78), is

$$\frac{\Delta\omega_{osc}}{\omega_{osc}} = \frac{\Delta V}{2V} + \frac{\Delta d}{d} \tag{13.86}$$

Finally, consider the effect of beam temperature on the microwave generation process where no resonant cavity is used, and therefore feedback is minimal. Beam temperature affects both bandwidth and efficiency. In the case of a foil diode, the electrons suffer energy losses and are scattered by the foil. This is in addition to the inherent beam temperature induced by the emission process, which is equivalent to having electrons of widely varying voltage interacting with the virtual cathode. Thus, an extremely broad RF spectrum is produced, which greatly reduces the detectable signal in any particular frequency band.

13.5.3 Nonresonant Vircator Design

A major impediment to constructing an efficient vircator is the effect of heating on the efficiency of microwave generation. As noted some time

ago by Birdsall and Bridges [3], beam temperature significantly damps out the amplitude of the potential oscillation. This can be understood in the following way. For a monoenergetic beam, all of the charged particles bunch at the same location. Mathematically, this represents a singularity, where the charge density goes to infinity. In reality, the charge bunch is not infinitely dense, but it does become several times greater than the initial beam-injection density. The severity of the charge bunching leads to efficient microwave generation. If, conversely, the beam has a spread in axial momentum, then the electrons will stop at different locations in the potential well, as shown in Figure 13.17 [69]. This tends to limit the charge bunching and the amplitude of the oscillating electric and magnetic fields. The effect of beam temperature in reducing the RF efficiency of a broad-bandwidth vircator has been witnessed in electromagnetic simulations [70]. A beam spread of less than 3% in energy reduces the microwave generation efficiency by an order of magnitude. Under these conditions, the vircator is nothing more than a Barkhausen oscillator [39]. Indeed, the low efficiency and broad bandwidth observed in nonresonant vircator experiments may be attributed in part to the effects of electron scattering from the foil and resultant increase in beam temperature.

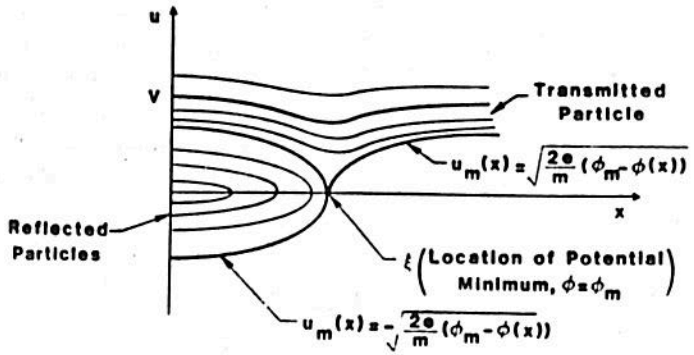

Fig. 13.17 Electron Flow Diagram for a Warm Beam

On the basis of our current understanding of vircator theory, the following characteristics should be designed into any experiment. The voltage pulse should be constant. For centimeter wavelengths, a foil diode or reflex triode can be used, employing a high-transparency mesh for the anode. To mimimize beam scattering, the mesh should be as thin as possible. In a foil diode or reflex triode, tuning is accomplished by changing the A-K gap spacing. Strong axial magnetic fields should be avoided in order to prevent electron reflexing over multiple passes, which can lead to beam heating via the two-stream instability.

For an injected current $I > I_{SCL}$, the oscillation frequency is given by (13.83). Because the oscillating beam is equivalent to a deformable dipole, the preferred waveguide mode for an axisymmetric beam in a straight-walled cylindrical guide is TM_{0n}, where $n \sim D/\lambda_0$, D is the waveguide diameter, and λ_0 is the free-space wavelength. This will place n at or near the mode closest to cut-off. Once n is known, we can determine the phase velocity, group velocity, wavelength, and impedance of the wave in the guide. Similar considerations hold for a rectangular waveguide. Note that both I_{SCL} and the cut-off wavelength λ_c depend on the guide's dimensions and geometry. Both must be considered when choosing an experimental configuration.

13.5.4 Foilless Diode Vircators

Foilless diodes represent a means of achieving millimeter wavelength microwaves from the vircator mechanism. The following points must be considered in the design of a coherent high-frequency vircator. First, generation of high microwave frequencies requires large beam densities. Extremely high beam densities ($n_0 > 10^{14}$ cm^{-3}) have been obtained from foilless diodes. Unlike foil diodes, the beam plasma frequency scales linearly with the electron-cyclotron frequency due to the magnetic field [71]. This is significant because it implies that a single vircator can be tuned over an order of magnitude in frequency (e.g., 10–100 GHz), simply by changing the axial magnetic field strength, without changing the physical structure of the device.

Second, as noted earlier, using a very large value of I/I_{SCL} does not substantially increase frequency or RF efficiency. A foilless diode in a strong axial magnetic field produces a very thin annular beam. Because I_{SCL} for an annular beam is larger than for a solid beam of the same area, the value of I/I_{SCL} will be smaller for the same beam current.

In order to ensure narrow-bandwidth and high-efficiency microwave generation in this configuration, minimal reflexing of electrons in the region between the real and virtual cathodes must occur. The two-stream instability greatly heats the beam electrons, which are tied to the B_z field lines. The axial magnetic field must be shaped to divert the electrons, or *flux excluders* must be employed to confine the magnetic field to the diode region. This arrangement allows the radial space-charge electric field to perform the role of expelling electrons to the waveguide wall. In addition, if the beam is annular, a collimator may be used to help prevent reflexing of electrons back to the cathode.

The requirement that the electron beam must be cold is met by the use of a foilless diode. Experimental [72] and theoretical [71] results indicate that foilless diodes create low-emittance beams. Laminar flow, where the electron's Larmor orbit is smaller than the beam thickness, is obtained when [72]:

$$\omega_c > (\gamma_0 - 1)^{1/2} \frac{c}{\sqrt{a\delta/2}} \tag{13.87}$$

where a is the orbital radius, δ is the radial spacing between the cathode and drift tube wall (which acts as the anode), and ω_c is the electron-cyclotron frequency given by eB_z/mc. Low beam scatter is also ensured because of the lack of a foil.

Finally, the diode voltage and injected current must be constant. More appropriately stated, the *impedance* must be constant. Flat-top voltage pulse can be attained in a variety of ways for several diode configurations. However, at high voltages, the foilless diode purely operates as a resistive load [71], and therefore $\omega_{osc} \propto \sqrt{I/V} = 1/\sqrt{Z}$ is constant. Also, the absence of diode closure in some foilless diode experiments makes a long-pulse device possible.

It is evident from our discussion that the foilless diode in a strong axial magnetic field represents the optimal configuration for a high-frequency vircator. This configuration optimizes microwave power and efficiency, while generating coherent high-frequency radiation. A design that incorporates all of these features was proposed several years ago [67, 73, 74], and is shown in Figure 13.18. The concept has recently been resurrected and is being pursued, as discussed by Kwan [75].

13.5.5 Electromagnetic Particle Simulations

The ultimate tool for designing vircator experiments is an electromagnetic particle-in-cell or PIC code. The 2-1/2 dimensional code CCUBE has been used extensively for this purpose. In conjunction with the detailed theory presented in this chapter, a small number of simulation runs will optimize the microwave generation from a given experiment. Figures 13.19 to 13.23 show typical output from a CCUBE simulation used to design the original MGX vircator experiment at Lawrence Livermore National Laboratories [68]. Such computer runs help define frequency, bandwidth, waveguide mode, and expected microwave power. Detailed comparisons of vircator experiments and simulations are presented in Chapter 14 by L. Thode.

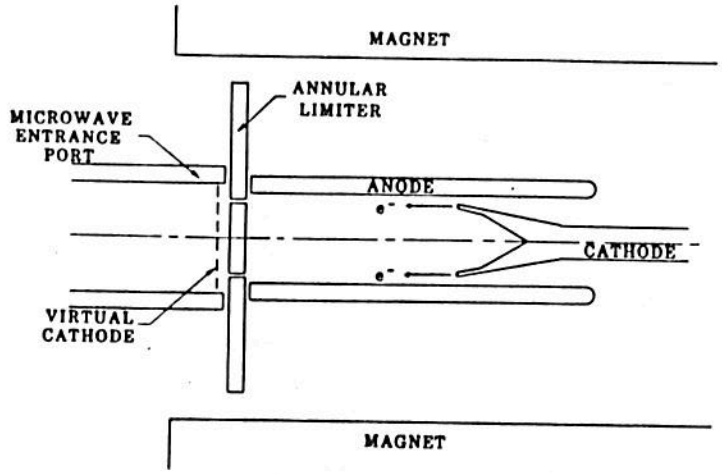

Fig. 13.18 Foilless Diode Vircator Design

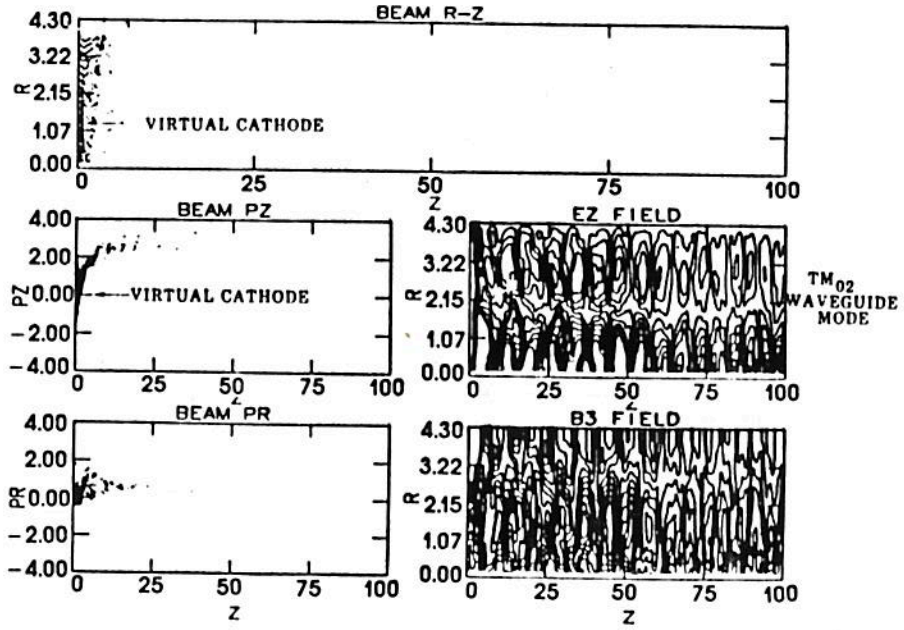

Fig. 13.19 Two-Dimensional EM Simulation of Multigigawatt Virtual Cathode Oscillator (Vircator) Tube (700 kV, 70 kA)

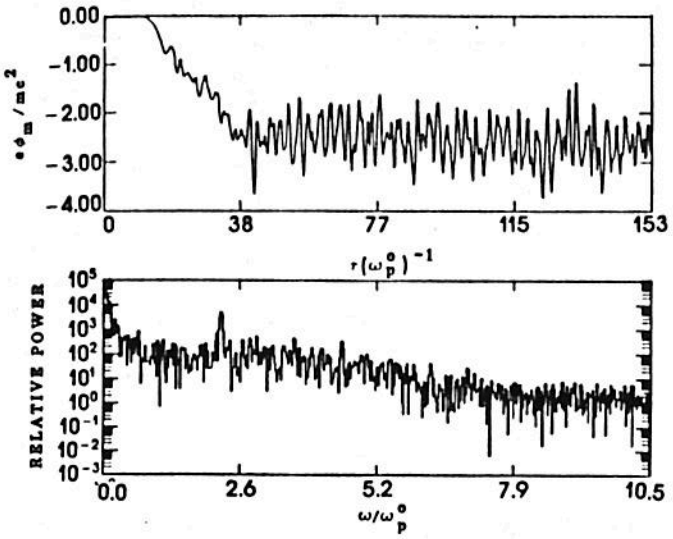

Fig. 13.20 Potential Variation and Power Spectrum in Virtual Cathode Region (700 kV, 70 kA)

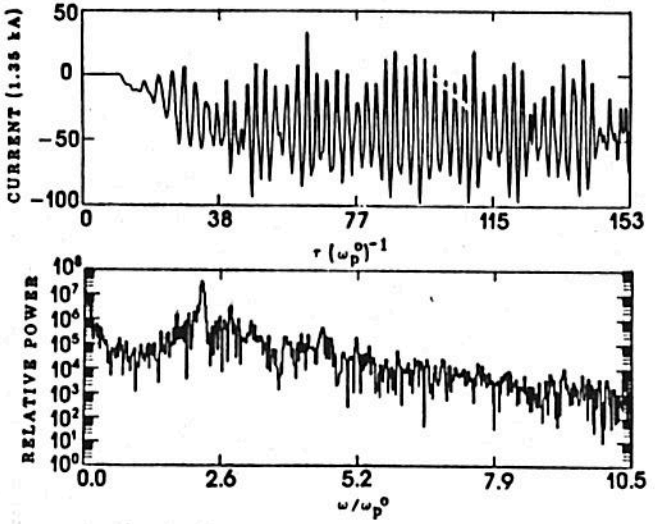

Fig. 13.21 Current Variation and Power Spectrum in Virtual Cathode Region (700 kV, 70 kA)

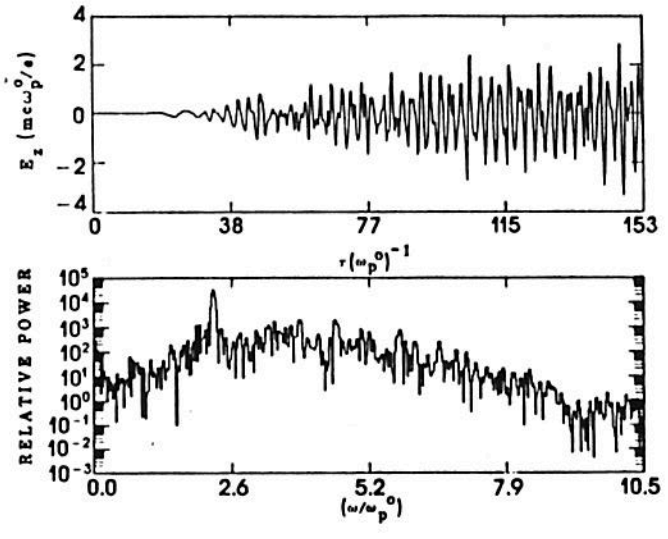

Fig. 13.22 Axial Electric Field in Waveguide (TM_{02} Mode) and Power Spectrum (700 kV, 70 kA)

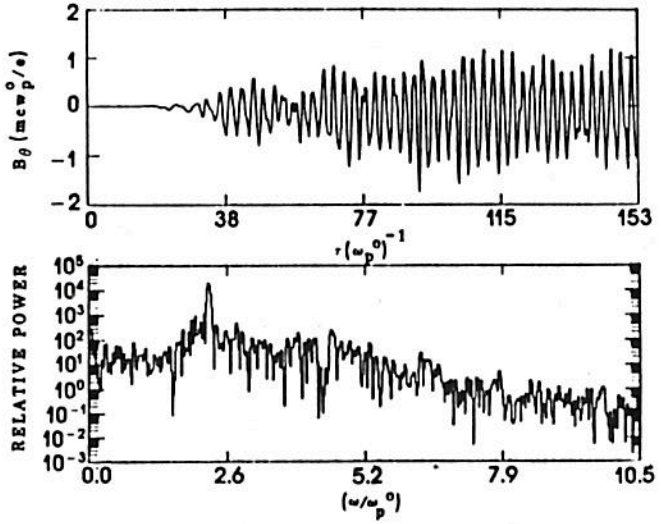

Fig. 13.23 Transverse Magnetic Field in Waveguide (TM_{02} Mode) and Power Spectrum (700 kA, 70 kA)

13.6 MICROWAVE GENERATION FROM THE RESONANT CAVITY VIRCATOR

As described in Section 13.5, a vircator without a resonant structure is a free-running oscillator. The microwave signal grows from noise at roughly $5/2\ \omega_p^{rel}$. Because of beam temperature, nonuniform beam current density, changing beam parameters during diode closure, and the large bandwidth of the instability where gain can occur, the vircator frequency can *and does* change rapidly, and often discontinuously, during the beam pulse. This results in lower gain and lower efficiency for two reasons. First, the gain-bandwidth product of a given device with fixed load is a constant. The vircator tends to have large bandwidth and moderate gain, similar to a reflex klystron. In contrast magnetrons and multiple cavity klystrons have extremely narrow bandwidths and high gain. The second reason, which is related to the first, is that the frequency changes so rapidly that the instability does not saturate, and the maximum gain is never obtained as a result.

In order for the vircator to reach its potential as a high-power source, a resonant structure must be used in order to trade off bandwidth for gain. Ideally, the resonant structure would allow only one cavity mode to grow over the bandwidth in which the vircator would normally have gain. The result is a single operating frequency in a given configuration. The resonant structure would be mechanically adjustable to the frequency of the source.

13.6.1 Theory

The resonant structure used in conjunction with the vircator may take many forms. These may include cylindrical cavities, iris loaded cavities, re-entrant coaxial cavities, re-entrant radial cavities, and radially or axially coupled cavities. These cavities may be of rectangular, circular, or generally cylindrical cross section. Likewise, the output or load may be variable. For example, radial wall loading may be used by employing loop or monopole antennas connected to a coaxial line, waveguide, or another cavity. The radial wall may be loaded directly by a waveguide or another cavity. Radial wall loading, however, leads to asymmetries in the mode pattern, especially if there is heavy output loading. Alternatively, the microwave power may be axially extracted by stub coupling, which maintains symmetry and has the added advantage of forming a natural coaxial transmission line for propagation of the microwaves in a transverse electromagnetic or TEM mode. For cylindrical geometry, this implies that only radial electric E_r and azimuthal magnetic B_θ fields would be present on the output line.

Of the various designs for cavities with output coupling considered to date, the simplest appears to be the most useful. This is a pill-box cavity with a cylindrical cross section. The unloaded resonant vircator is depicted in Figure 13.24. For simplicity, let us assume that the cross section is circular, rather than arbitrary. In the figure, d is the anode-cathode (A-K) gap spacing, r is the cathode radius, b is the diode wall radius, h is the height of the resonator, and r is the radius of the resonator. The microwaves may be radially extracted through a waveguide, or axially extracted by coupling to a coaxial stub. In order to allow for coupling between the A-K gap region and the cavity, the anode may not be a continuous screen mesh or foil. For instance, it may have a hole in the center, or an open annular region at the outer edge where it connects to the radial wall.

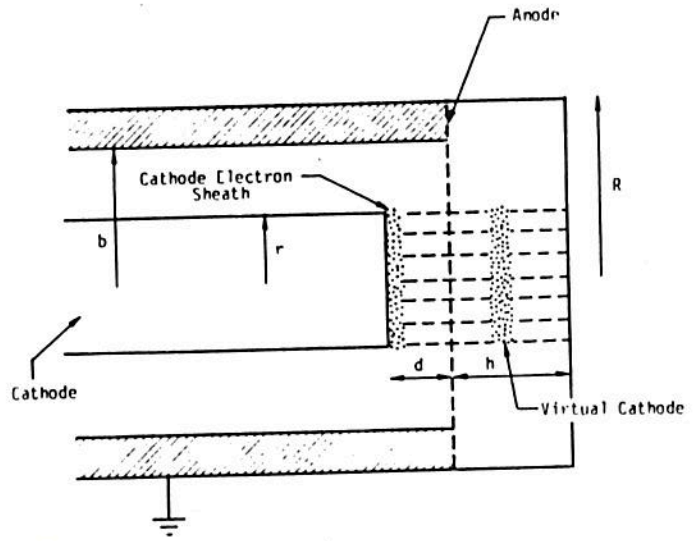

Fig. 13.24 Simple Resonant Cavity Structure for Vircator

The design of the resonant cavity vircator would proceed in the following way. Although it is not necessary, and may not be allowed by physical constraints on its size and shape or the voltage breakdown thresholds of materials, it is nonetheless desirable that the impedance of the diode match as closely as possible the impedance of the pulse-forming line or network in order to maximize power flow. If we assume that the diode may be approximated as planar ($r \gg d$) and that the voltage is not highly relativistic, then the Child-Langmuir relation may be used to define r and d:

$$Z = \frac{V}{I} = \frac{V}{j_{CL} \cdot \text{area}}$$

$$= \frac{V}{2.34 \times 10^{-6} \dfrac{V^{3/2}}{d^2} \pi r^2} \tag{13.88a}$$

or

$$Z(\Omega) = 136 V^{-1/2} (d/r)^2 \tag{13.88b}$$

where V is in megavolts, and d and r are in the same units. Other formulations should be used for highly relativistic beams [4].

The values of r and d are determined by the choice of frequency. The frequency of oscillation can be written as

$$f_{osc}\,(\text{GHz}) = 10.2 \sqrt{j(\text{kA/cm}^2)/\beta\gamma} \tag{13.89}$$

by using (13.74) and (13.80), the relation:

$$n_b = 2.08 \times 10^{11}\, j(\text{kA/cm}^2)/\beta \tag{13.90}$$

and the values of e and m. By substituting the Child-Langmuir relation in the form:

$$j_{CL}\,(\text{kA/cm}^2) = 2.34 V^{3/2}\,(\text{MV})/d^2\,(\text{cm}) \tag{13.91}$$

for the current density, we have uniquely defined the value of d, and therefore r, for the desired frequency.

The cavity geometry is set by two factors. The first is to have the resonant frequency of the cavity equal to the frequency of maximum gain for the space-charge instability. This is given by (13.89). The second factor is to have only one mode with a resonant frequency in the bandwidth where the space-charge instability has significant gain. The resonant cavity frequency for vacuum cylindrical cavity of circular cross section is

$$f_{mnp}\,(\text{GHz}) = 4.775 \sqrt{\frac{X_{mn}^2}{r^2} + \frac{p^2\pi^2}{h^2}} \tag{13.92}$$

where r and h are in centimeters; m, n, and p are integers, which can take on values of $m = 0, 1, 2, 3, \ldots$, $n = 1, 2, 3, \ldots$, and $p = 0, 1, 2, 3, \ldots$; X_{mn} is the nth root of $J_m(X) = 0$ for TM and $J'_m(X) = 0$ for TE cavity modes. Of course, J_m is the Bessel function of order m, and J'_m is its derivative.

One way to ensure that only one cavity mode grows is to choose cavity dimensions whereby only the lowest order mode has a frequency in the gain bandwidth. Vircators in the cylindrical geometry discussed here can generate TM modes. Because of the strong charge bunching in the virtual diode section, the $p = 0$ mode (constant E_z field) is not possible. Finally, given azimuthal symmetry, we expect $m = 0$. Therefore, TM_{011} is the lowest order cavity mode of interest. Another method would be to attempt to place the higher order modes far enough apart so as to have large growth in only one mode.

Finally, there is the load on the resonator system. The load should be set to allow as much microwave power output from the cavity as possible, consistent with the provision of sufficient feedback to have high gain for the instability and the prevention of RF vacuum breakdown. The entire question of optimizing the cavity load is a major one for the system efficiency, and needs to be researched in detail.

To summarize, a resonant cavity vircator would work as follows. An electron beam is accelerated in the real diode, and injected into the resonant cavity with a certain energy and current density. This determines the frequency of oscillation. Because the beam is first accelerated, it can be seen that the vircator is more analogous to a klystron than other space-charge microwave generators, such as microwave triodes or lighthouse tubes [76]. As the electrons form a virtual cathode and begin to oscillate, they receive a very strong feedback from the cavity at one particular frequency. This forces the oscillator to be locked in frequency. The feedback overcomes the natural tendency of the vircator toward frequency shifting and mode hopping due to the large bandwidth of the space-charge instability. With a narrow effective bandwidth and the mode competition eliminated, the gain of the device is much larger, and it is allowed to saturate at a single frequency. The proximity of the output load to the virtual cathode allows for strong coupling.

13.6.2 Reflex Triode Resonant Cavity Experiment

A resonant vircator experiment was conducted on the Pulserad PR112A. The experimental configuration is schematically represented in Figure 13.25. The anode and cathode were arranged in a reflex triode geometry (cathode at ground, anode at positive voltage). The experiment

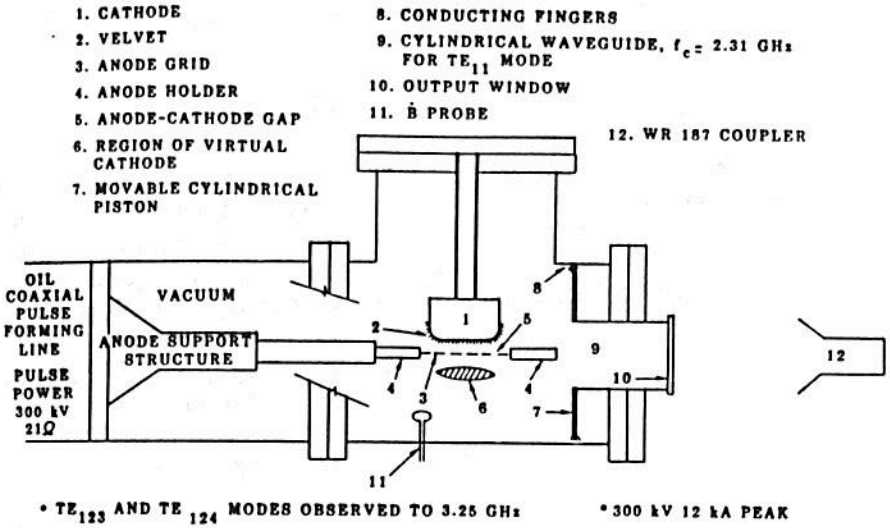

Fig. 13.25 Schematic of Reflex Triode Geometry for Resonant Vircator Experiment on the PR112A

is similar to the Soviet one, which was accomplished in rectangular waveguide [25]. The major difference is the addition of a moveable piston to tune the cavity.

At the proper spacing, the TE_{124} mode was observed with a resonant frequency of 3.25 GHz. By moving the piston toward the pulser by a half-wavelength, the TE_{123} mode was witnessed with the same frequency. The usual frequency-chirping characteristic of a free-running vircator returned when the beam voltage was changed so that the vircator was no longer resonant with the cavity. This behavior is shown in Figure 13.26, recorded by a *polar frequency discriminator* (PFD). When the two traces (horizontal and vertical signal components) maintain the same ratio of amplitudes, the frequency is a constant as in Figure 13.26(b, c). In contrast, the frequency in Figure 13.26(d) is changing from 3.30 to 3.67 GHz. This implies a bandwidth of greater than 10% over the microwave pulse.

The hollow waveguide in the center of the piston was chosen to couple out a TE_{11} waveguide mode from the TE_{123} cavity mode. The radiation pattern for a TE_{11} mode is a solid, horizontally polarized, almost uniformly illuminated circle, which is ideal for testing. The TE_{11} output mode was verified by the light pattern excited in fluorescent bulbs and the plane of polarization of the *E*-field. The total output power was not measured

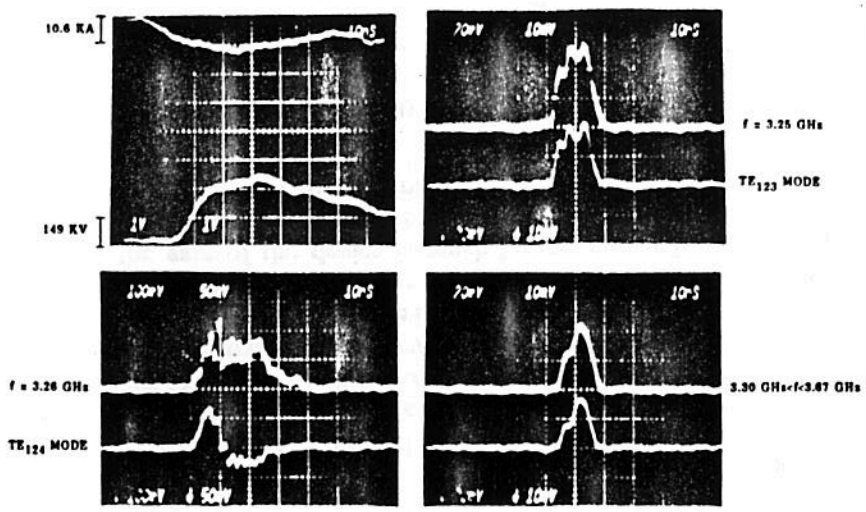

Fig. 13.26 (a) Current (top) and Voltage (bottom) on the Triode; PFD Data Showing Resonant Oscillation (b) at 3.26 GHz and (c) 3.25 GHz; (d) Frequency Sweeping from 3.30 GHz to 3.67 GHz

because the lucite forming the vacuum-air interface over the three-inch diameter waveguide breaks down, and air breakdown has been witnessed as well. However, the microwave detector measures 110 kW/cm^2 at 25 cm distance and the fluorescent bulbs light up uniformly over a diameter of two feet, thus indicating high power. Also, a B-dot probe on the cavity wall to measure B_z indicates a power density in excess of 10 MW/cm^2. This is especially significant because the total input beam power is only 3.6 GW (300 kV, 12 kA). The efficiency could conceivably approach 10% as in the Soviet experiment [25].

REFERENCES

1. G.D. Child, *Phys. Rev. Ser. I* **32**, 492 (1911).
2. I. Langmuir, *Phys. Rev.* **21**, 419 (1923).
3. C.K. Birdsall and W.B. Bridges, *Electron Dynamics of Diode Regions* (Academic Press, New York 1966), Chapter 3.
4. H.R. Jory and A.W. Trivelpiece, *J. Appl. Phys.* **40**, 3924 (1969).
5. V.S. Voronin, Yu. T. Zozulya and A.N. Lebedev, *Zh. Tekh. Fiz.*

42, 546 (1972); *Sov. Phys.-Tek. Phys.* **17**, 432 (1972).
6. R.J. Lomax, *Proc. IEE Pt. C* **108**, 119 (1961).
7. C.E. Fay, A.L. Samuel, and W. Shockley, *Bell Syst. Tech. J.* **17**, 49 (1938).
8. C.K. Birdsall and W.B. Bridges, *J. Appl. Phys.* **32**, 2611 (1961).
9. W.B. Bridges and C.K. Birdsall, *J. Appl. Phys.* **34**, 2946 (1963).
10. D.A. Dunn and I.T. Ho, *A.I.A.A.J.* **1**, 2770 (1963).
11. S.A. Goldstein and R. Lee, *Bull. APS* **23**, 763 (1978).
12. R.A. Meyer, S.A. Goldstein, D.D. Hinshelwood, and G. Cooperstein, *Bull. APS* **24**, 977 (1979).
13. D.S. Prono, J.M. Creedon, I. Smith, and N. Bergstrom, *J. Appl. Phys.* **46**, 3310 (1975).
14. D.S. Prono, J.W. Shearer, and R.J. Briggs, *Phys. Rev. Lett.* **37**, 2 (1976).
15. P.A. Miller, J.A. Halbleib, J.W. Poukey, and J.T. Verdeyen, *J. Appl. Phys.* **52**, 593 (1981).
16. J.W. Poukey and N. Rostoker, *Plasma Phys.* **13**, 897 (1971).
17. C.L. Olson, "Collective Ion Acceleration with Linear Electron Beams," in *Collective Ion Acceleration-Springer Tracts in Modern Physics*, Vol. 84, (Springer-Verlag, 1979).
18. C. L. Olson, *IEEE Trans. Nucl. Sc.* **NS-26**, 4231 (1979).
19. C.L. Olson, J.R. Woodworth, C.A. Frost, and R.A. Gerber, *IEEE Trans. Nucl. Sc.* **NS-28**, 3349 (1981).
20. R.B. Miller, in *Proc. 2nd Int. Top. Conf. on High Power Electron and Ion Beam Research and Technology* (Cornell University, Ithaca, NY, 1977), p. 613.
21. R.B. Miller, in *Collective Methods of Acceleration*, N. Rostoker and M. Reiser, eds. (Harwood Academic Publishers, Geneva, 1979), p. 675.
22. R.A. Mahaffey, P. Sprangle, J. Golden, and C.A. Kapetanakos, *Phys. Rev. Lett.* **39**, 843 (1977).
23. H.E. Brandt, A. Bromborsky, H.B. Bruns, and R.A. Kehs, in *Proc. 2nd Int. Top. Conf. on High Power Electron and Ion Beam Research and Technology* (Cornell University, Ithaca, NY, 1977), p. 649.
24. J.M. Buzzi, H.J. Doucet, B. Etlicher, P. Haldenwang, A. Huetz, H. Lamain, C. Rouille, J. Cable, J. Delvaux, J.C. Jouys, and C. Peugnet, *ibid.*, p. 663.
25. A.N. Didenko, G.P. Fomenko, I.Z. Gleizer, Ya.E. Krasik, G.V. Melnikov, S.F. Perelygin, Yu.G. Shtein, A.S. Sulakshin, V.I. Tsvetkov, and A.G. Zerlitsin, *ibid.*, p. 683.
26. D.J. Sullivan, in *Proc. 3rd Int. Top. Conf. on High Power Electron and Ion Beam Research and Technology* (Institute of Nuclear Physics, Novosibirsk, USSR, 1979), p. 769.

27. D.J. Sullivan, *Bull. APS* **25**, 948 (1980).
28. D.J. Sullivan, D.E. Voss, W.M. Bollen, R.H. Jackson, and E.A. Coutsias, AMRC-R-451 (1983), unpublished.
29. D.E. Voss, D.J. Sullivan, G.F. Kiuttu, R.J. Adler, and J. Walsh, *Bull. Am. Phys. Soc.* **29**, 1285 (1984).
30. T.J.T. Kwan and L.E. Thode, *Phys. Fluids* **27**, 1570 (1984).
31. S. Burkhardt, R. Scarpetti, and R.L. Lundberg, *J. Appl. Phys.* **58**, 28 (1985).
32. A. Bromborsky, H. Brandt, and R.A. Kehs, *Bull. APS* **26**, 165 (1981); private communication.
33. M.C. Clark, private communication.
34. A.N. Didenko, A.G. Zherlitsyn, A.S. Sulakshin, G.P. Fomenko, V.I. Tsvetkov, and Yu. G. Shteyn, *Pisma v. Zhur. Tek. Fiz.* **9**, 1510 (1983).
35. H.A. Davis, R.R. Bartsch, L.E. Thode, E.G. Sherwood, and R.A. Stringfield, *Phys. Rev. Lett.* **55**, 2293 (1985).
36. J. Benford, H. Sze, W. Woo, and B. Harteneck, *Phys. Rev. Lett.* **56**, 334 (1986).
37. R. Espinosa, *1984 Microwave System Design Handbook* (1983), p. 126.
38. H. Hertz, *Wied. Ann.* **19**, 87 (1893).
39. H. Barkhausen and K. Kurz, *Phys. Zeit.* **21**, 1 (1920).
40. W.E. Benham, *Phil. Mag.* **5**, 641 (1928).
41. F.B. Llewellyn and A.E. Bauen, *Bell Syst. Tech. J.* **18**, 280 (1939).
42. V.A. Flyagin, A.V. Gaponov, M.I. Petelin, and V.K. Yulpatov, *IEEE Trans.* **MTT-25**, 514 (1977).
43. S. Jacobs, *et al.*, *Physics of Quantum Electronics*, Vol. 5, (Addison-Wesley, Reading, MA, 1978).
44. S. Jacobs, *et al.*, *Physics of Quantum Electronics*, Vol. 7, (Addison-Wesley, Reading, MA, 1980).
45. D.J. Sullivan, G.F. Kiuttu, R.J. Adler, D.E. Voss, and J. Walsh, *Phase I Report: Resonant Vircator Study*, Mission Research Corporation, AMRC-R-654, (1984), unpublished.
46. In addition to the obvious communication and research applications, there is a very large range of industrial processing applications (See Ref. [37]).
47. The general value of α follows from the ratio of losses to the useful output.
48. L.A. Bogdankevich and A.A. Rukhadze, *Sov. Phys. Upsekhi* **14**, 163 (1971).
49. B.N. Brejzman and D.C. Ryutov, *Nucl. Fusion* **14**, 875 (1974).
50. T.C. Genoni and W.A. Proctor, *J. Plasma Phys.* **23**, 129 (1980).
51. R.B. Miller and D.C. Straw, *J. Appl. Phys.* **47**, 1897 (1976).

52. J.R. Thompson and M.L. Sloan, *Proc. 2nd Int. Conf. on High Power Electron and Ion Beam Research and Technology* (Laboratory for Plasma Studies, Cornell University, Ithaca, NY, October 1977), Vol. II, p. 734, Eq. (14).
53. B.B. Godfrey, *J. Comp. Phys.* **15**, 504 (1974).
54. B.B. Godfrey, *J. Comp. Phys.* **19**, 58 (1975).
55. R.B. Miller and D.C. Straw, *J. Appl. Phys.* **48**, 1061 (1977).
56. L.E. Thode, B.B. Godfrey, and W.R. Shanahan, *Phys. Fluids* **22**, 747 (1979).
57. R.Z. Sagdeev, in *Reviews of Plasma Physics*, Vol. 4, M.A. Leontovich, ed. (Consultants Bureau, 1966), p. 23.
58. S.S. Moiseev and R.Z. Sagdeev, *Plasma Phys.* **5**, 43 (1963).
59. E.A. Coutsias and D.J. Sullivan, *Phys. Rev. A* **27**, 1535 (1983).
60. D.J. Sullivan and E.A. Coutsias, in *High Power Beams '81*, H.J. Doucet and J.M. Buzzi, eds. (Ecole Polytechnique, Paris, 1981), p. 371.
61. J.R. Pierce, *J. Appl. Phys.* **15**, 721 (1944).
62. J.W. Poukey, J.P. Quintenz, and C.L. Olson, *Appl. Phys. Lett.* **38**, 20 (1981).
63. B.B. Godfrey, Mission Research Corporation, AMRC-R-282 (1981), unpublished.
64. J. Kevorkian and J.D. Cole, *Perturbation Methods in Applied Mathematics* (Springer-Verlag, Berlin, 1981).
65. G. Birkhoff and G. Rota, *Ordinary Differential Equations* (Ginn, New York, 1962).
66. A.V. Paschenko and B.N. Rutkevich, *Fiz. Plazmy* **3**, 774 (1977); *Sov. J. Plasma Phys.* **3**, 437 (1977).
67. D.J. Sullivan, *IEEE Trans. Nucl. Sc.* **NS-30**, 3426 (1983).
68. R. Scarpetti, R.L. Lundberg, and S.C. Burkhardt, *Bull. APS* **29**, 1180 (1984).
69. E.A. Coutsias, *J. Plasma Phys.* **31**, 313 (1984).
70. M.A. Mostrom, T.J.T. Kwan, and C.M. Snell, *Bull. APS* **27**, 1075 (1982).
71. M.E. Jones and L.E. Thode, *J. Appl. Phys.* **51**, 5212 (1980).
72. R.B. Miller, K.R. Prestwich, J.W. Poukey, and S.L. Shope, *J. Appl. Phys.* **51**, 3506 (1980).
73. D.J. Sullivan, "A High Power Microwave Generator," US Air Force Invention No. 13,692, US Patent Pending, 1979.
74. D.J. Sullivan, "High Power Microwave Generator Using Relativistic Electron Beam in Waveguide Drift Tube," US Patent No. 4,345,220, August 17, 1982.
75. T.J.T. Kwan, *Phys. Rev. Lett.* **57**, 1895 (1986).

76. D.R. Hamilton, J.K. Knipp, and J.B. Horner Kuiper, *Klystrons and Microwave Triodes*, (Dover, New York, 1966).